Cell Reports

Article

Saturated fatty acids dampen the immunogenicity of cancer by suppressing STING

Graphical abstract

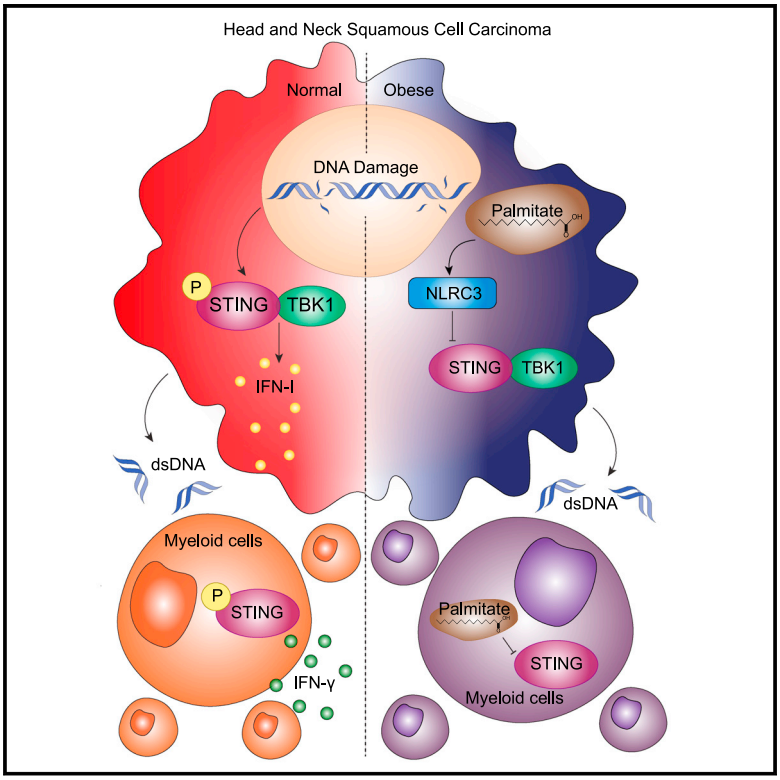

Highlights

- Obesity establishes an IFN-I-deprived tumor microenvironment and increases tumor burden
- Myeloid cells from obese hosts are desensitized to STING stimulation
- Saturated fatty acids inhibit the STING pathway by inducing NLRC3
- NLRC3 inhibits the immunogenicity of HNSCC in an IFN-I-dependent fashion

Authors

Blake R. Heath, Wang Gong, Hülya F. Taner, ..., Yuying Xie, James J. Moon, Yu Leo Lei

Correspondence

leiyuleo@umich.edu

In brief

The STING-type-I interferon pathway underpins immune surveillance against cancers. However, how metabolic comorbidity contributes to STING suppression is unclear. Heath et al. find that myeloid cells from obese hosts are desensitized to STING. Saturated fatty acids can inhibit STING by inducing NLRC3, dampening the immunogenicity of cancers.

Heath et al., 2023, Cell Reports *42*, 112303
April 25, 2023
https://doi.org/10.1016/j.celrep.2023.112303

CellPress

Cell Reports

CellPress
OPEN ACCESS

Article

Saturated fatty acids dampen the immunogenicity of cancer by suppressing STING

Blake R. Heath,[1,2,13] Wang Gong,[2,3,13] Hülya F. Taner,[2,4,13] Luke Broses,[2,3] Kohei Okuyama,[2,3] Wanqing Cheng,[2] Max Jin,[5] Zackary R. Fitzsimonds,[2] Andriana Manousidaki,[6] Yuesong Wu,[6] Shaoping Zhang,[7] Haitao Wen,[8] Steven B. Chinn,[3,9] Eric Bartee,[10] Yuying Xie,[6] James J. Moon,[1,3,11,12] and Yu Leo Lei[1,2,3,4,9,14,*]

[1]Graduate Program in Immunology, University of Michigan Medical School, Ann Arbor, MI, USA
[2]Department of Periodontics and Oral Medicine, University of Michigan, Ann Arbor, MI, USA
[3]University of Michigan Rogel Cancer Center, Ann Arbor, MI, USA
[4]Graduate Program in Oral Health Sciences, University of Michigan School of Dentistry, Ann Arbor, MI, USA
[5]Homer Stryker M.D. School of Medicine, Western Michigan University, Kalamazoo, MI, USA
[6]Department of Computational Mathematics, Science, and Engineering, Department of Statistics, Michigan State University, East Lansing, MI, USA
[7]Department of Periodontics, University of Iowa College of Dentistry, Iowa City, IA, USA
[8]Department of Microbial Infection and Immunity, Ohio State University, Columbus, OH, USA
[9]Department of Otolaryngology-Head and Neck Surgery, University of Michigan Health System, Ann Arbor, MI, USA
[10]Department of Internal Medicine, Division of Molecular Medicine, University of New Mexico Health Sciences Center, Albuquerque, NM 87131, USA
[11]Department of Pharmaceutical Sciences, University of Michigan College of Pharmacy, Ann Arbor, MI 48109, USA
[12]Department of Biomedical Engineering, University of Michigan College of Engineering, Ann Arbor, MI 48109, USA
[13]These authors contributed equally
[14]Lead contact
*Correspondence: leiyuleo@umich.edu
https://doi.org/10.1016/j.celrep.2023.112303

SUMMARY

Oncogenes destabilize STING in epithelial cell-derived cancer cells, such as head and neck squamous cell carcinomas (HNSCCs), to promote immune escape. Despite the abundance of tumor-infiltrating myeloid cells, HNSCC presents notable resistance to STING stimulation. Here, we show how saturated fatty acids in the microenvironment dampen tumor response to STING stimulation. Using single-cell analysis, we found that obesity creates an IFN-I-deprived tumor microenvironment with a massive expansion of suppressive myeloid cell clusters and contraction of effector T cells. Saturated fatty acids, but not unsaturated fatty acids, potently inhibit the STING-IFN-I pathway in HNSCC cells. Myeloid cells from obese mice show dampened responses to STING stimulation and are more suppressive of T cell activation. In agreement, obese hosts exhibited increased tumor burden and lower responsiveness to STING agonist. As a mechanism, saturated fatty acids induce the expression of *NLRC3*, depletion of which results in a T cell inflamed tumor microenvironment and IFN-I-dependent tumor control.

INTRODUCTION

Immune checkpoint blockade (ICB) has recently become the first-line treatment for multiple types of solid tumors, including head and neck squamous cell carcinomas (HNSCCs). In contrast to the decline of overall cancer incidence in the United States, the cancer burden of HNSCC continues to increase and will maintain an upward trend until the year 2060.[1,2] This is largely driven by the prevalence of human papillomavirus (HPV)-associated oropharyngeal squamous cell carcinomas (OPSCC). OPSCCs have very high mutational burdens and frequently contain HPV16 viral epitopes, which cannot evade immune detection through central immune tolerance. However, its response to ICB is usually below 15%.[3,4] This clinical observation suggests that the immunogenicity of OPSCC is controlled by mechanisms beyond the presence of immunogenic epitopes. Understanding the mechanisms underpinning cancer immunogenicity is pivotal to developing strategies to sensitize hypoimmunogenic cancers to immune killing.

Recently, we found that cancer cell-specific expression of an adaptor molecule for type-I interferon (IFN-I) activation, stimulator of interferon genes (STING), is a strong positive prognosticator in HNSCC patients.[5] In addition, when HNSCC cells became resistant to effector immune cell-mediated killing, multiple inhibitors of the STING-IFN-I pathway were upregulated in cancer cells.[6] Indeed, the proper activation of IFN-I is essential for the expression of MHC Class I molecules and antigen presentation.[7,8] These findings suggest that the fitness of STING-mediated innate immune surveillance in the HNSCC tumor microenvironment (TME) is essential for the detection and control of cancers.

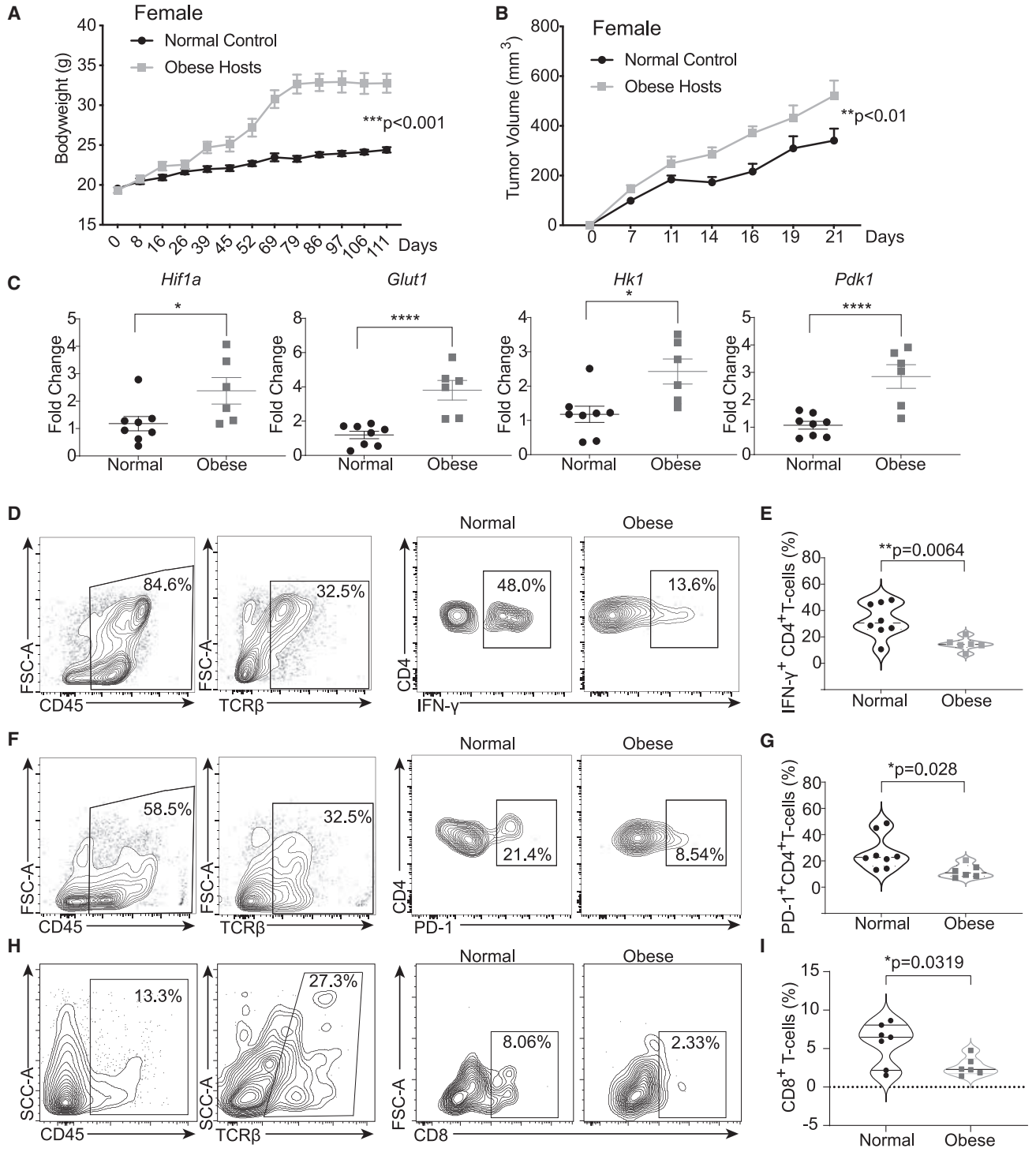

Figure 1. Obesity exacerbates intra-tumoral hypoxic stress and inhibits effector T cell function

(A) To establish the obesity model, six-week-old female C57BL/6 mice were fed either a normal (11.4% kcal fat) or high-fat (60% kcal fat) diet for twelve weeks prior to tumor implantation and monitored for weight for the duration of the experiment (n = 16 normal-weight and n = 14 obese mice). Bodyweight differences between groups were assessed using the generalized estimating equation model (***p < 0.001).

(B) One million MOC2-E6/E7 cancer cells were implanted subcutaneously into the right flank of normal-weight and obese mice and monitored for tumor growth (n = 16 normal-weight and n = 14 obese mice). Tumors were measured every 2–4 days. Tumor burden between groups was compared using the generalized estimating equation model (**p < 0.01). Obesity *in vivo* experiments were performed twice (n = 24 normal-weight and n = 20 obese mice).

(legend continued on next page)

Priming strategies that aim to reinvigorate innate immune sensing are being extensively tested in preclinical models, and many have advanced into phase 1/2 clinical trials to sensitize hypoimmunogenic cancers to ICB. For example, radiotherapy has recently emerged as a promising priming treatment modality for HNSCC.[9–11] Notably, the success of radiotherapy depends on intact STING signaling with defects in the STING pathway dampening radiotherapy-induced sensitization to immune killing.[12,13] HNSCC resistance to the combination of radiotherapy and immunotherapy has been an emerging pivotal challenge.[14] Thus, it is important to identify mechanisms that lead to STING insufficiency in HNSCC.

Driver oncogenes frequently keep STING activation in check to facilitate immune escape. For example, HPV16 E7 can facilitate the protein turnover of STING by engaging NLRX1-dependent autophagosomes.[5] As an independent oncogenic event, in about 20% of HNSCCs, the amplification of the 3q26.3 genetic locus is present with the co-amplification of *SOX2* and *PIK3CA*. Similar to HPV16 E7, SOX2 can also destabilize STING through autophagy-dependent machinery.[6] The consequent IFN-I-deprived tumors show features of hypoimmunogenicity, such as resistance to ICB and decreased diversity of T cell receptors.[15] Thus, the identification of key checkpoints of STING is critical to understanding the HNSCC adaptive resistance to innate immune priming. In addition, intra-HNSCC myeloid cells are typically devoid of epithelial oncogenes, and the mechanisms shaping their response plasticity to STING stimulation remain insufficiently characterized.

Metabolic dysregulation has recently emerged as a major underlying condition affecting HNSCC incidence and response to therapies. The link between obesity and the risks for several types of gastrointestinal tract, breast, esophageal, and endometrial cancers has been extensively studied; however, the impact of obesity on HNSCC was not well characterized until recently. Evidence from several large independent cohorts in different continents suggests that obesity is a previously underappreciated risk factor for HNSCC. In the NIH-AARP diet and health prospective cohort involving 218,854 participants and a Spain prospective cohort involving 3.5 million adults, obesity was a significant risk factor for HNSCC.[16,17] A similar finding was made in a cohort involving about 6.7 million patients in South Korea.[18] Among patients who were positive for HPV, the risk of OPSCC was increased with higher body mass index values.[19] HNSCC patients, especially the HPV$^+$ OPSCC population, who took statins to reduce cholesterol levels showed improved clinical outcomes.[20,21] Overall, these findings suggest that obesity is a significant risk factor for HNSCC initiation and escape from the immune system.

In this study, we aimed to characterize the molecular mechanism underpinning obesity-potentiated immune escape of HNSCC. We mapped the anti-tumor immune response in obese hosts at single-cell resolution and found that obese hosts establish an IFN-I-deprived tumor microenvironment with significantly increased HNSCC burden. We and others have shown that STING agonists exhibit potent therapeutic potential for HNSCC.[6,8,22–24] However, STING agonists lost effectiveness in obese tumor-bearing hosts. Bone-marrow-derived macrophages (BMDMs) and peritoneal macrophages from obese mice were insensitive to STING stimulation. In agreement, the myeloid-derived suppressor cells (MDSC) derived from bone marrow and those from the TME in obese hosts were more suppressive of effector T cell activation. We found that saturated fatty acids, but not unsaturated fatty acids, inhibited IFN-I signaling through the upregulation of NLRC3, a recently identified DNA-binding protein that suppresses the STING pathway. We further showed that NLRC3 sensed saturated fatty acids and inhibited HNSCC immunogenicity in an IFN-I signaling-dependent fashion. Overall, this study describes a molecular link between obesity and cancer cell escape from innate immune sensors and identifies a central metabolic pathway that controls HNSCC immunogenicity.

RESULTS

Obesity exacerbates intra-tumoral hypoxic stress and inhibits effector T cell function

To understand the effects of obesity on tumor burden and the TME, we first established an obese mouse model by feeding four- to six-week-old C57BL/6 female mice either a normal chow diet (consisting of 11.4% kcal fat content) or a 60% kcal high-fat diet for twelve weeks,[25] and monitored mouse weights weekly (Figure 1A). After twelve weeks, we used the MOC2-E6/E7 syngeneic HNSCC tumor model, which does not respond to ICB monotherapies.[5,6] One million MOC2-E6/E7 cells were implanted subcutaneously into the right flank of mice fed either normal chow or a high-fat diet and monitored for tumor burden starting one week following implantation. We found that obese mice displayed a significantly higher tumor burden in relation to normal control mice (Figure 1B). Hypoxia is a key feature of the HNSCC TME, which shows a median partial pressure of oxygen (pO_2) of 9 mm Hg, in contrast with a pO_2 of 40–60 mm Hg in the paired normal tissue.[26] Hypoxia drives autophagy to switch the dominant metabolism from oxidative phosphorylation to glycolysis.[27–30] We resected tumors from control and obese hosts and homogenized tissue for qPCR analysis of the glycolysis pathway markers. We found the tumors from obese mice displayed even higher levels of *Hif1a*, *Glut1*, *Hk1*, and *Pdk1* (Figure 1C). It has been previously shown that effector T cell function requires sufficient extracellular glucose support to sustain rapid

(C) Total RNA was isolated from one representative set of whole excised tumors. The transcripts of the glycolysis pathway intermediates *Glut1*, *Hk1*, *Pdk1*, and *Hif1a* were quantified via qPCR (n = 8 normal-weight mice; n = 6 obese mice). Values represent mean ± SEM of three technical replicates per tumor. All comparisons between two groups were made using a two-tailed unpaired *t* test (*p < 0.05 and ****p < 0.0001).
(D–G) Tumor-infiltrating lymphocytes from one representative set of experiments were analyzed by flow cytometry. The gating strategy was as follows: lymphocytes, singlets, live cells (Zombie Aqua negative), CD45$^+$, TCRβ^+, and CD4$^+$. The frequencies of IFNγ^+CD4$^+$ and PD-1$^+$CD4$^+$ T cells were analyzed by flow cytometry (n = 8 normal-weight mice; n = 6 obese mice). All comparisons between two groups were made using a two-tailed unpaired *t* test (**p < 0.01).
(H and I) Tumor-infiltrating CD8$^+$ T cells were analyzed using flow cytometry (n = 7 lean mice; n = 6 obese mice). Comparisons between the two groups were made using a two-tailed unpaired *t* test (**p < 0.01).

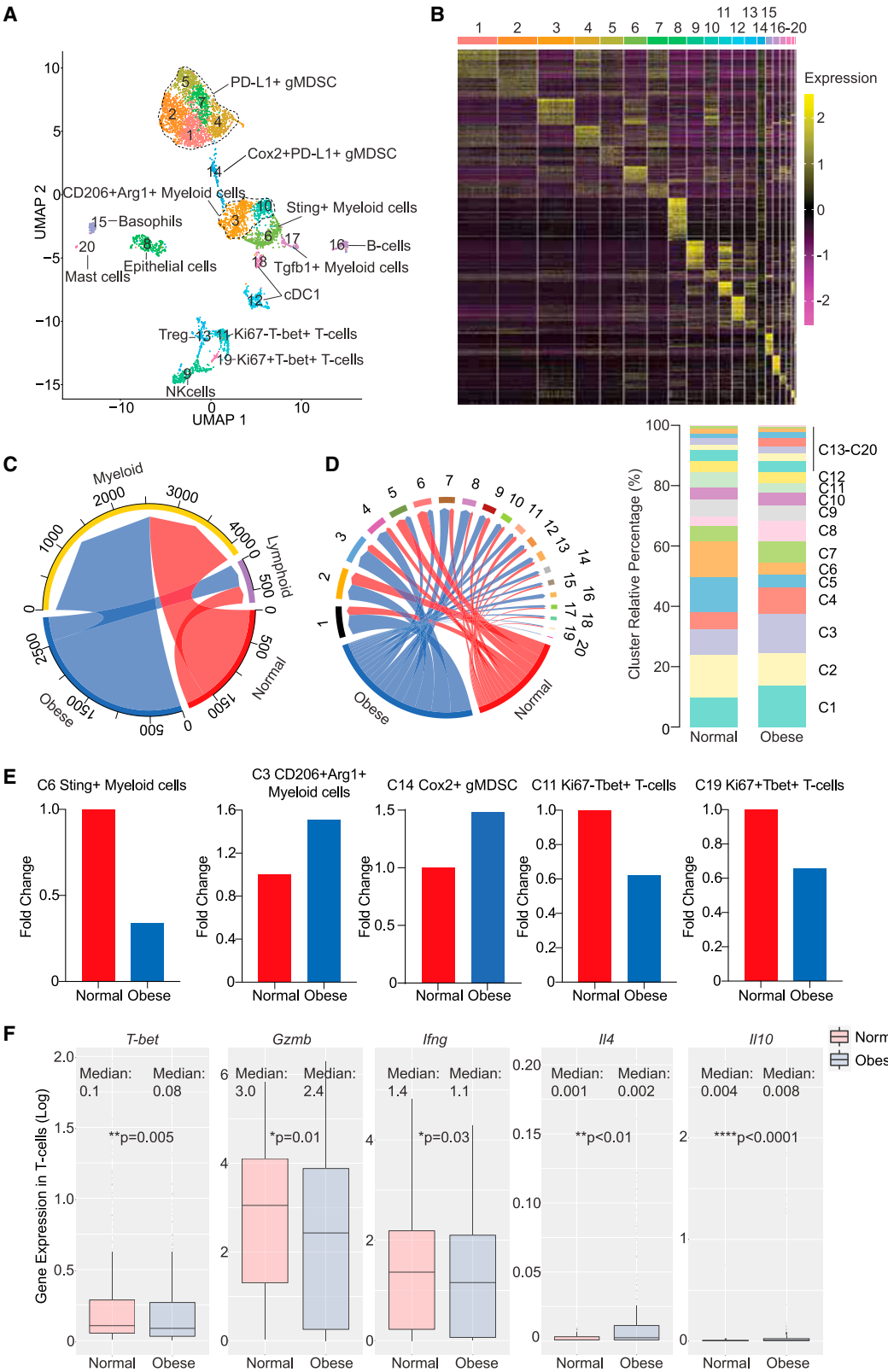

(legend on next page)

genome replication, cytokine synthesis, and cytotoxic cargo delivery, and that a lack of metabolic support results in T cell exhaustion.[31–35] As the tumors from obese hosts were even more glycolytic, we assessed the effector function of tumor-infiltrating lymphocytes (TILs). We purified TILs using the Ficoll-Paque gradient and stimulated them with PMA/ionomycin. We found that tumors from obese hosts contained fewer IFN-γ^+CD4$^+$ T cells (Figures 1D and 1E). Our prior study using human HNSCC tissue suggests that PD-1$^+$ T cells are activated effectors.[36,37] We found that tumors from obese mice also contained fewer PD-1$^+$CD4$^+$ T cells (Figures 1F and 1G). In agreement, the overall frequency of CD8$^+$ T cells was significantly lower in tumors grown in obese mice (Figures 1H and 1I).

Obesity establishes an intra-tumoral immune landscape that dampens Th1 polarization

The generation of effector T cells is the culmination of a series of immunological reactions starting from the activation of antigen-presenting cells. To characterize obesity-associated TME alteration at a high resolution, we harvested five tumors from the control diet group and five tumors from the high-fat diet group. After we sorted out live CD45$^+$ immune cells from the tumor single-cell suspension, we mixed about an equal number of immune cells from each tumor sample together to ensure a balanced representation. The two pools of TILs were then subjected to single-cell RNA sequencing (scRNA-seq). After filtering, we integrated 5,154 high-quality transcriptomes and identified 20 distinct cell clusters (Figure 2A). Most of the TILs in the MOC2-E6/E7 model consisted of four suppressive myeloid cell subsets with complementary features. The first suppressive myeloid subset included clusters 1, 2, 4, 5, and 7. These MDSCs expressed high levels of *Ly6g* and *PD-L1*. The second subset, cluster 14, consisted of granulocytic MDSCs with high expression levels of *Cox2*. The third myeloid cell subset consisted of clusters 3 and 10 and was defined by high expression levels of *CD206* and *Arginase 1* (*Arg1*). The fourth suppressive myeloid cell subset cluster 17 expressed high levels of *Tgfb1* but low levels of *PD-L1*. In addition, there were two myeloid cell subsets that were maintained by IFN-I signaling. The first subset was cluster 6 with high expression levels of *Sting*, *CD40*, *CD86*, and IFN-I target genes, such as *Cxcl9*, *Cxcl10*, *Isg15*, and *Mx1*. The other subset was conventional dendritic cell type 1 (cDC1), which included clusters 12 and 18. There were only a limited pool of T cells (clusters 11, 13, and 19), consistent with the hypoimmunogenic nature of this model. Each cluster was associated with a distinct transcriptional profile (Figure 2B, Table S1).

Next, we examined the relative percentage of the myeloid and lymphoid compartments. High-fat-diet-induced obesity triggered myeloid compartment expansion and lymphoid clusters contraction in the TME (Figures 2C and 2D). Specifically, we found that the activated myeloid cells with high expression levels of *Sting* and IFN-I signatures were reduced by 66.1% in tumor-associated myeloid cells (TAMs) from obese mice, representing a reduction of 11.9% of total infiltrating immune cells in the regular diet group to 4.0% in the high-fat diet group (Figure 2E). In contrast, there was a 50.8% increase in CD206$^+$Arg1$^+$ TAMs (cluster 3), a 48.7% increase in Cox2$^+$ granulocytic MDSCs (cluster 14), and a 20% contraction of an IFN-I-maintained cDC1 subset (cluster 18) in TILs from obese mice. Ki67$^-$T-bet$^+$ effector T cells (cluster 11) and Ki67$^+$T-bet$^+$ effector T cells (cluster 19) were reduced by 37.8% and 34.5% in the TILs from obese hosts, respectively (Figure 2E). To better assess the effector functional state of intra-tumoral T cells, we first compared the expression of *T-bet*, a master transcription factor for Th1 development. Intra-tumoral T cells from obese hosts expressed lower levels of *T-bet*. The median expression levels of *Gmzb* and *Ifng* in T cells isolated from tumors in obese mice were 25.1% and 50.1% of those in the TILs from lean hosts. In contrast, the levels of Th2 cytokines, such as *Il4* and *IL10*, in T cells from TILs in obese mice were higher (Figure 2F).

Saturated fatty acids, but not unsaturated fatty acids, dampen STING-mediated immune activation

As our immune profiling of HNSCC from normal and obese mice suggests that obesity leads to an IFN-I-deprived phenotype, we next sought to investigate the mechanism of obesity-mediated Th1 suppression. Palmitate, an ester of palmitic acid, is used to model the effects of obesity.[38–40] Palmitate accounted for 61% of the total saturated fatty acids in the high-fat diet. To examine both cancer cell and immune cell responsiveness to saturated fatty acids, we pretreated both MOC2-E6/E7 cells and BMDMs with either carrier alone, i.e., 10% bovine serum albumin (BSA), or 200 μM palmitate-BSA for 24 h, as previously described[40,41] for 24 h. We previously showed that MOC2-E6/E7 cancer cells express HPV16 E7, which promotes the turnover of STING, and are inert to STING agonists, cyclic dinucleotides (CDNs) and that STING protein needs to be expressed to bypass intrinsic cancer suppression of this pathway.[5,6] Indeed, the relative expression of STING levels was much lower in MOC2-E6/E7 cells than BMDMs (Figure S1A). Thus, we transfected 1.0 μg/mL STING expression plasmid in MOC2-E6/E7 cells 16 h prior to qPCR analysis of the IFN-I gene signatures including *Ifnb1*,

Figure 2. Obesity establishes an intra-tumoral immune landscape that dampens Th1 polarization

(A) Tumors from normal-weight and obese mice were harvested at day 21 after implantation. CD45$^+$ tumor-infiltrating immune cells were FACS sorted and pooled (n = 5 mice/condition) and subjected to single-cell RNA sequencing. After filtering, 5,154 high-quality transcriptomes were integrated for UMAP analysis. Divergent myeloid, lymphoid, and epithelial lineages were defined by the top 2,025 genes with the highest cell-to-cell variation.

(B) Clusters displayed from (A) showed distinct gene expression patterns.

(C) The size of myeloid and lymphoid compartments in TILs separated from lean and obese hosts are shown.

(D) The absolute size (left) and relative percentage of each cluster (right) in TILs separated from lean and obese mice are shown.

(E) The frequencies of cluster 6 (STING$^+$ myeloid cells), cluster 3 (CD206$^+$Arg1$^+$ M2-like macrophages), and cluster 14 (Cox2$^+$ granulocytic MDSCs), as well as clusters 11 and 19 (Tbet$^+$ T cells) are shown for TILs separated from lean control and obese mice.

(F) The expression levels (Log) of *Tbet*, *Gzmb*, *Ifng*, *Il4*, and *Il10* were compared between T cells (clusters 11, 13, and 19) in TILs separated from lean control and obese mice using the R-package stats (*$p < 0.05$, **$p < 0.01$, ****$p < 0.0001$).

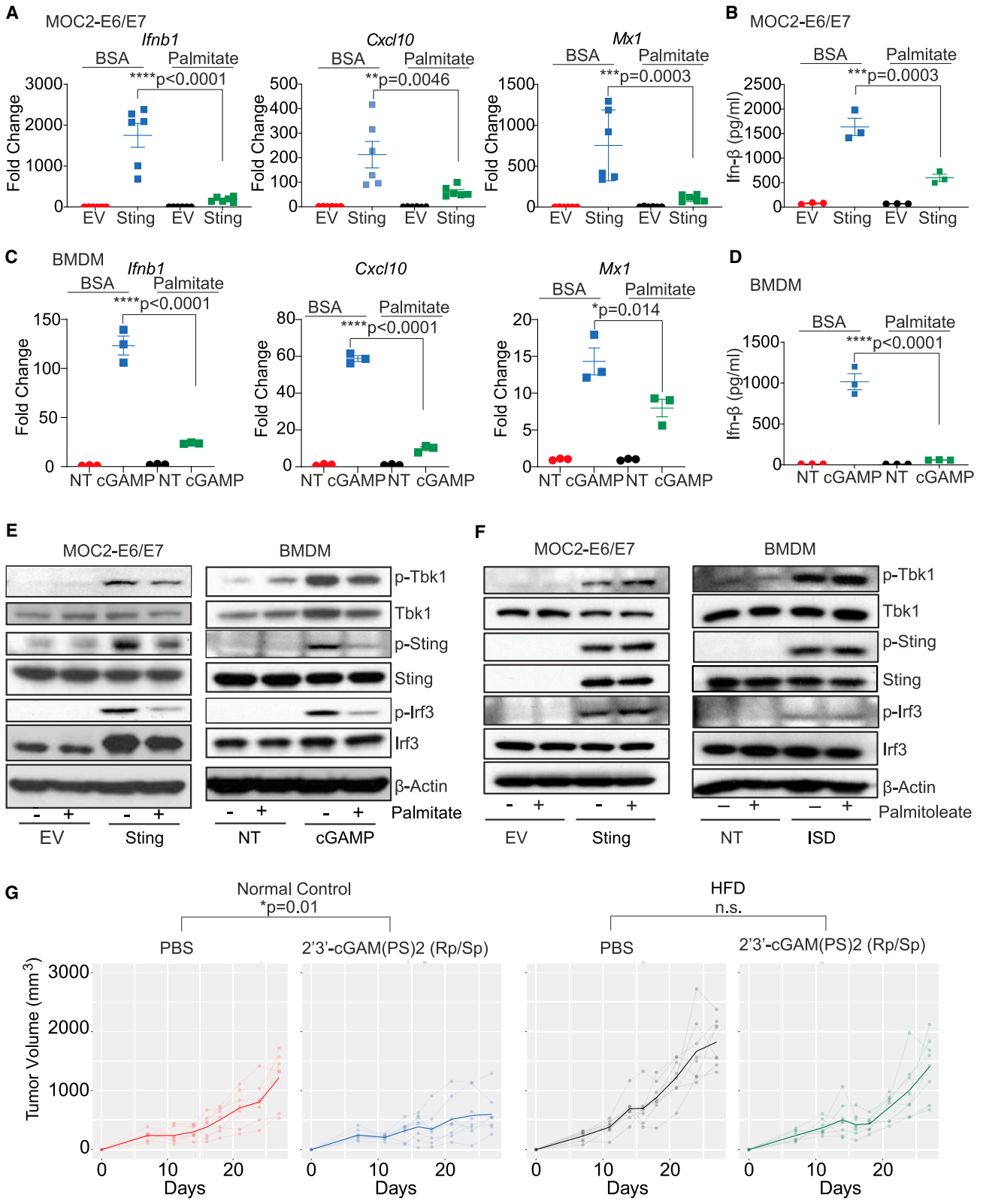

(legend on next page)

Cxcl10, and *Mx1*. We found that STING expression induced high levels of transcription of *Ifnb1* and its target genes *Cxcl10* and *Mx1*, as expected. Palmitate nearly abrogated STING-mediated cytokines transcription (Figure 3A). To substantiate the finding, we performed ELISA of the supernatant and found that palmitate significantly inhibited STING-induced IFN-β production (Figure 3B). Intra-HNSCC TAMs do not suffer from epithelial oncogenes-mediated STING suppression. Thus, we then generated BMDMs to test the effect of palmitate on CDNs-induced immune activation. We transfected BMDMs with 1.0 μg/mL cyclic di-GMP-AMP (cGAMP) and incubated for 16 h. Consistent with our findings in tumor cells, palmitate significantly inhibited cGAMP-induced gene transcription and nearly abrogated IFN-β protein production, as measured by qPCR and ELISA, respectively (Figures 3C and 3D). To characterize STING signaling, we performed immunoblots using lysates from treated MOC2-E6/E7 cells and BMDMs. We found that palmitate reduced the hallmarks of STING activation, including the phosphorylation of TBK1, IRF3, and STING (Figure 3E). To assess whether this link is unique to palmitate, we also treated MOC2-E6/E7 cells and BMDMs with 200 μM myristate, which is another common form of saturated fatty acids in the experimental high-fat diet. Then, we expressed STING in MOC2-E6/E7 cells and treated BMDMs with cGAMP to induce STING signaling. Myristate exposure suppressed the phosphorylation of Tbk1, Sting, and Irf3, similar to palmitate incubation (Figures S1B and S1C).

To assess the specificity of saturated fatty acid-mediated suppression of the STING-IFN-I pathway, we tested whether unsaturated fatty acids can also regulate this pathway. Palmitoleic acid is a monounsaturated ω-7 fatty acid. It is one of the most common unsaturated fatty acids in the experimental high-fat diet and adipose tissue. As with palmitate, we treated MOC2-E6/E7 cells with BSA alone or 200 μM palmitoleate-BSA for 24 h, followed by transfection of 1.0 μg/mL STING expression plasmid. Palmitoleate incubation had no effect on STING-mediated IFN-I signaling (Figure 3F). We also incubated BMDMs with 200 μM palmitoleate for 24 h and transfected cells with 2.0 μg/mL STING agonist. Palmitoleate did not reduce the phosphorylation of Tbk1, Sting, and Irf3 (Figure 3F). Then, we sought to determine whether this observation could be extrapolated into other unsaturated fatty acids. Oleic acid is a monounsaturated ω-9 fatty acid found in various dietary sources. As with palmitate, we treated MOC2-E6/E7 cells with carrier alone or 200 μM oleate-BSA for 24 h, followed by transfection of 1.0 μg/mL STING expression plasmid. We found that oleate did not affect STING-mediated IFN-I response (Figure S1D). Similarly, we incubated BMDMs with 200 μM oleate for 24 h and then transfected cells with 1.0 μg/mL cGAMP. Oleate did not modulate the magnitude of CDN-mediated immune activation (Figure S1E).

Although STING-inducing therapies have entered clinical trials, as either a single agent or a priming agent for ICB, it remains unclear whether underlying conditions, such as obesity, affect cancer response. Thus, we tested the effectiveness of a modified cGAMP, 2′3′-cGAM(PS)$_2$, in our established HNSCC obesity model. 2′3′-cGAM(PS)$_2$ was engineered to contain stereoisomers of phosphorothioate diester linkages, which are resistant to the hydrolysis activities of ENPP1. 2′3′-cGAM(PS)$_2$ has shown significantly improved anti-tumor activity *in vivo*.[42] Mice were fed either a regular chow diet (consisting of 11.4% kcal fat content) or a 60% kcal high-fat diet for twelve weeks prior to implantation of MOC2-E6/E7 tumor cells. Then, we treated mice intratumorally (i.t.) with either PBS or 2.5 μg 2′3′-cGAM(PS)$_2$ seven days post-implantation, once per week for three weeks. In agreement with previous reports, intra-tumoral injection of 2′3′-cGAM(PS)$_2$ reduced tumor burden in mice on the regular diet. Six of seven mice showed a response. The therapeutic effectiveness was reduced significantly in tumor-bearing obese mice (Figure 3G). Collectively, these data suggest that saturated fatty acids, but not unsaturated fatty acids, have a profound negative impact on the activation of the STING-IFN-I pathway and that obesity negatively affects the therapeutic effectiveness of CDNs *in vivo*.

Myeloid cells from obese hosts were insensitive to STING stimulation and were more suppressive to T cell activation

So far, we have shown that obesity expands the quantity of TAMs and saturated fatty acids dampen the STING response in normal myeloid cells *in vitro*. Next, we sought to characterize the quality of TAMs and myeloid cells separated from obese mice. The experimental high-fat diet model has known sexual dimorphism.[43] To make sure our observed tumor burden difference is consistent between both sexes, we established a lean and obese male mice model using the same method described above. Mouse weights were monitored longitudinally for more than 100 days and the high-fat diet group showed significantly more weight gain during the observation window (Figure 4A). In

Figure 3. Saturated fatty acids, but not unsaturated fatty acids, dampen STING-mediated immune activation

(A and B) MOC2-E6/E7 cells were pretreated with mock (BSA only) or 200 μM palmitate-BSA for 24 h then transfected with 1.0 μg/mL mouse Sting expression plasmid for 16 h. (A) RNA was isolated and expression of murine *Ifnb1*, *Cxcl10*, and *Mx1* was assessed via qPCR. The experiment was repeated twice, and values represent mean ± SEM of six biological replicates per sample. (B) Supernatant was collected and assessed for the presence of IFN-β via ELISA. Values represent mean ± SEM of three technical replicates per sample. All comparisons were made using one-way ANOVA (**p < 0.01; ***p < 0.001; ****p < 0.0001).

(C and D) Bone marrow-derived macrophages (BMDMs) were pretreated with mock (BSA only) or 200 μM palmitate-BSA for 24 h then transfected with 1.0 μg/mL 2′3′-cGAMP for 16 h. (C) RNA was isolated and expression of murine *Ifnb1*, *Cxcl10*, and *Mx1* was assessed via qPCR. Values represent mean ± SEM of three biological replicates per sample. (D) Supernatant was collected and assessed for the presence of IFN-β via ELISA. Values represent mean ± SEM of three technical replicates per sample. All comparisons were made using one-way ANOVA (*p < 0.05; ****p < 0.0001).

(E and F) MOC2-E6/E7 cells and BMDMs were primed with BSA only, 200 μM palmitate-BSA (E), or 200 μM palmitoleate-BSA (F) for 24 h and then transfected with the indicated STING agonists, 1.0 μg/mL mouse Sting, 1.0 μg/mL 2′3′-cGAMP, or 2.0 μg/mL ISD for 16 h. Cell lysates were subjected to SDS-PAGE for the indicated markers.

(G) One million MOC2-E6/E7 cancer cells were implanted subcutaneously into the right flank of normal-weight or obese mice 12 weeks post-high-fat diet feeding. One week later, either mock (PBS, 100 μL) or 2.5 μg 2′3′-cGAM(PS)$_2$ (Rp/Sp) was administered to mice i.t. once per week for 3 weeks. Tumors were measured every 2–4 days starting day 7 post-implantation. Tumor growth curves are compared among the groups (*p = 0.01, n.s. p > 0.05).

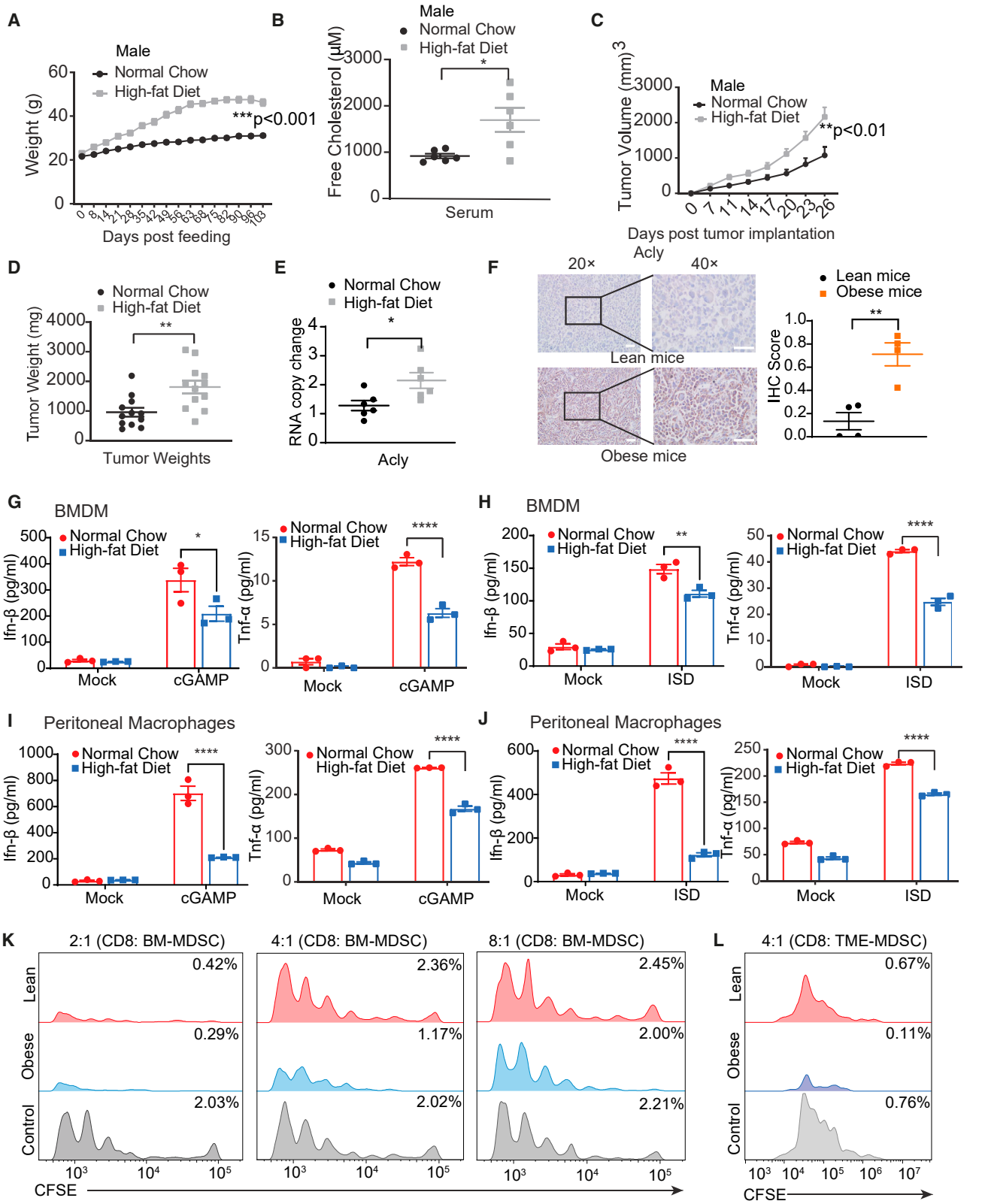

(legend on next page)

addition, the mice from the high-fat diet group showed significantly elevated cholesterol levels in the serum (Figure 4B). Livers were harvested from mice in the lean and obese groups and stained with a lysochrome, oil red O, to quantitate fat deposition. As expected, there was significantly more fat accumulation in the livers of obese mice, further validating the model (Figure S2). Twelve weeks post-high-fat diet treatment, we implanted MOC2-E6/E7 tumors and found that obese mice suffered from a significantly higher tumor burden, consistent with the female mouse model (Figures 4C and 4D). To ensure that there is also increased fatty acid biosynthesis in the TME, we resected tumors and quantitated the levels of ATP citrate synthase (Acly) at both transcription and protein levels. We found that tumors from obese mice expressed higher levels of *Acly* (Figure 4E). In agreement, both tumor cells and infiltrating immune cells showed stronger Acly staining (Figure 4F), suggestive of elevated fatty acids synthesis in the TME of obese mice.

To better characterize the functional alteration of myeloid cells from obese hosts, we first generated BMDMs from bone marrows isolated from tumor-bearing lean and obese mice. We transfected the BMDMs with 2.0 μg/mL cGAMP and measured the levels of secreted IFN-β and tumor necrosis factor (TNF)-α in the supernatant by ELISA. The BMDMs from obese mice showed significantly lower levels of IFN-β and TNF-α, in response to cGAMP (Figure 4G). To further corroborate the findings, we transfected BMDMs from lean and obese mice with another STING agonist, 3.0 μg/mL interferon stimulatory DNA (ISD). BMDMs from obese mice showed significantly reduced transcription of IFN-I signatures, including *Ifnb1*, pan-*Ifna*, *Cxcl10*, *Isg15*, *Isg54*, and *Mx1* (Figure S3A). In agreement, we found that BMDMs from obese mice produced significantly lower levels of IFN-β and TNF-α (Figure 4H). During the one-week differentiation period to generate BMDMs, the cells from the obese group were not exposed to any additional saturated fatty acids. To ensure direct physiological relevance, we also separated peritoneal macrophages from tumor-bearing lean and obese mice. We first transfected them with 2.0 μg/mL cGAMP and found an even more dramatic reduction in STING-induced IFN-β secretion from peritoneal macrophages in the obese group (Figure 4I, left panel). Similarly, the peritoneal macrophages from obese mice were less capable of producing TNF-α, in response to cGAMP (Figure 4I, right panel). Then, we transfected the peritoneal macrophages from lean and obese mice with 3.0 μg/mL ISD and recapitulated our findings with BMDMs (Figure 4J). Interestingly, obesity-associated myeloid cell insensitivity was specific to STING stimulation. Next, we transfected BMDMs and peritoneal macrophages isolated from tumor-bearing lean and obese mice with 1.0 μg/mL 5′ppp-dsRNA, which specifically activates MAVS- but not STING-mediated IFN-I production, and incubated for 16 h. We did not see a difference between the cells from lean and obese mice (Figure S3B).

Finding that myeloid cells from obese mice are insensitive to STING stimulation, we next sought to characterize the functional profiles of MDSCs, which were expanded in the TME from obese hosts. Using a previously described protocol,[44] we generated bone marrow-derived MDSCs (BM-MDSCs) by culturing bone marrow cells for four days with 200 U/mL GM-CSF. This treatment licensed cells into monocytes predisposed to suppression. Monocytes were then activated using a combination of 0.1 μg/mL lipopolysaccharide (LPS) and 100 U/mL IFN-γ for 16 h. BM-MDSCs were purified by fluorescence-activated cell sorting (FACS) of live $CD11b^+Ly6g^+$ cells. We separated $CD8^+$ T cells from the spleens of age-matched C56BL/6J mice, which were then labeled with 5.0 μM CFSE. BM-MDSCs were co-cultured with $CD8^+$ T cells at 2:1, 4:1, and 8:1 ratios and treated with anti-CD3/CD28 beads. Following a four-day co-culture, a very high number of BM-MDSCs (2:1) ratio from either group can repress $CD8^+$ T cell proliferation, with the BM-MDSCs from obese mice being more suppressive (Figure 4K, left panel). The BM-MDSCs from obese mice also showed more suppressive activity than those separated from lean mice when co-cultured with $CD8^+$ T cells at 4:1 and 8:1 ratios. To validate this finding, we FACS sorted MDSCs from the tumors grown in lean and obese mice (TME-MDSC) and co-cultured them with purified

Figure 4. Myeloid cells from obese hosts were insensitive to STING stimulation and were more suppressive of T cell activation

(A) Six-week-old male C57BL/6 mice were fed either a normal (11.4% kcal fat) or high-fat (60% kcal fat) diet for twelve weeks prior to tumor implantation. Body weights were monitored for >100 days (n = 12 in regular diet group and n = 12 in high-fat diet group). Body weight differences between groups were assessed using the generalized estimating equation model (**$p < 0.001$).

(B) Serum samples were collected from both groups and free cholesterol levels measured (*$p < 0.05$).

(C) One million MOC2-E6/E7 cancer cells were then implanted subcutaneously into the right flank of the mice. Tumor size was measured every 2–4 days. Tumor burden between groups was compared using the generalized estimating equation model (*$p < 0.01$).

(D) Tumors were harvested and weighed (**$p < 0.01$).

(E) Total RNA was isolated from excised pieces of tumors. The transcripts of *Acly* were quantified via qPCR (n = 6 lean mice; n = 6 obese mice). Values represent mean ± SEM of three technical replicates per tumor (*$p < 0.05$).

(F) Immunohistochemistry (IHC) was performed to assess the protein levels of Acly in tumors grown in lean and obese mice. IHC was scored by ImageJ. Scale bar, 200 μm. Values represent mean ± SEM of four representative staining per group. The comparison between the two groups was made using a two-tailed unpaired t test (**$p < 0.01$).

(G–J) BMDMs (G and H) and peritoneal macrophages (I and J) from lean and obese mice were transfected with 2.0 μg/mL cGAMP or 3.0 μg/mL ISD and incubated for 16 h. The supernatants were collected from each group and assessed for the protein levels of secreted IFN-β and TNF-α using ELISA. Values represent mean ± SEM of three technical replicates per sample. The experiment was repeated to confirm all findings. Comparisons were made using two-way ANOVA, followed by multi-comparison tests (*$p < 0.05$, **$p < 0.01$, ****$p < 0.0001$).

(K) BM-MDSCs from lean (n = 4) and obese (n = 4) mice were cultured in 200 U/mL GM-CSF media for 4 days and then activated using 0.1 μg/mL LPS and 100 U/mL IFN-γ for 16 h. CFSE-labeled $CD8^+$ T cells were co-cultured with BM-MDSCs for 4 days and then analyzed by flow cytometry for proliferating $CFSE^+CD8^+$ T cells.

(L) TME-MDSCs were isolated from lean (n = 5) and obese (n = 6) tumor-bearing mice using FACS of $CD11b^+Ly6G^+$ cells. TME-MDSCs were co-cultured with CSFE-labeled $CD8^+$ T cells for 4 days and then analyzed by flow cytometry for proliferating $CFSE^+CD8^+$ T cells.

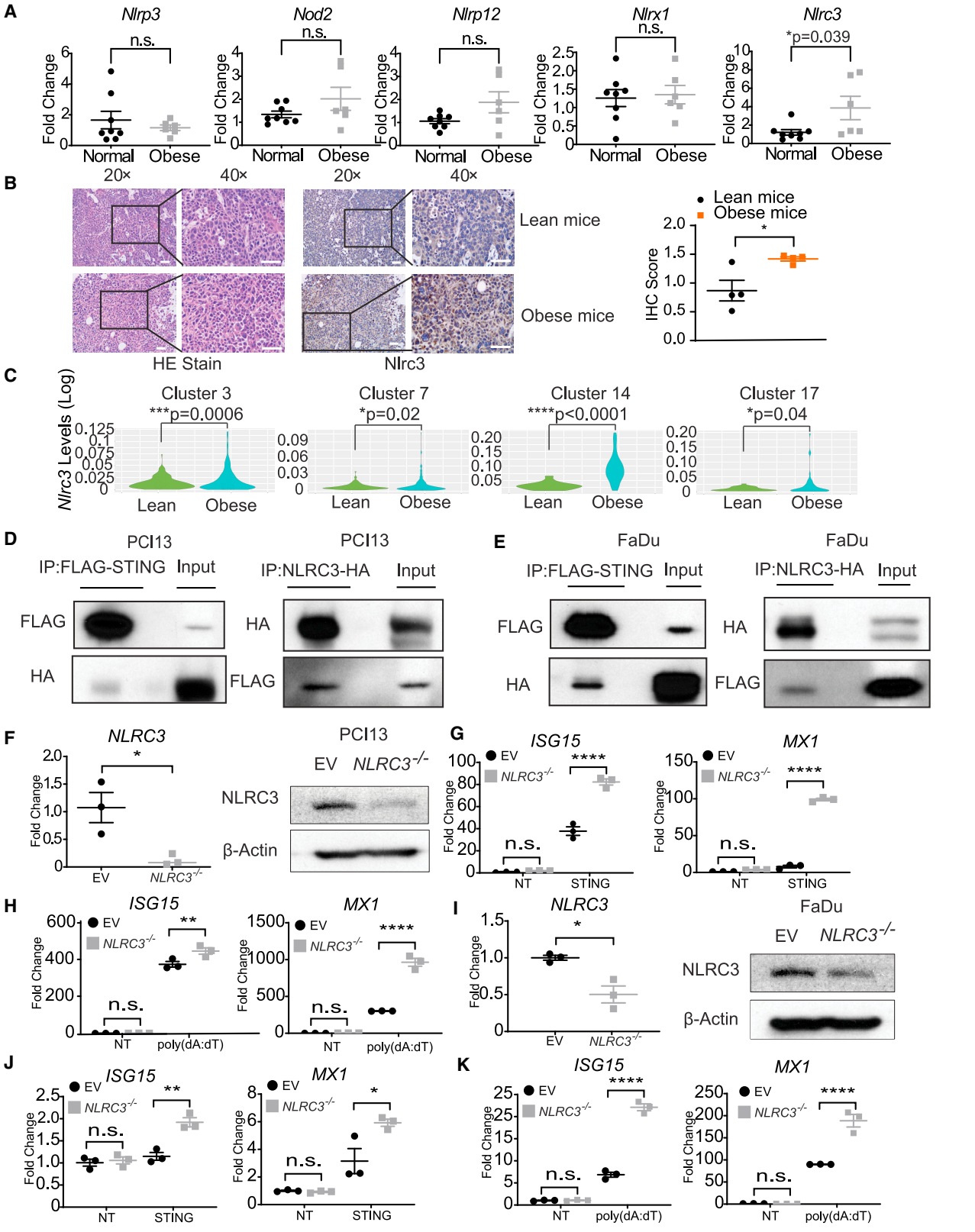

(legend on next page)

$CD8^+$ T cells at a 4:1 ratio. We found that the TME-MDSCs from tumors grown in obese mice were much more suppressive than those from the tumors grown in lean mice (Figure 4L).

Saturated fatty acids induce the expression of NLRC3 to antagonize STING signaling

To identify a molecular link that underpins saturated fatty acids-potentiated suppression of the STING-IFN-I response, we examined a panel of nucleotide-binding, leucine-rich repeats-containing (NLR) genes, which have emerged as central regulators of innate immune response and metabolism.[45–47] We extracted RNA from homogenized tumors from control and obese mice and assessed two pro-inflammatory *Nlr* genes (*Nlrp3* and *Nod2*) and three anti-inflammatory regulator *Nlr* genes (*Nlrp12*, *Nlrx1*, and *Nlrc3*). These *Nlr* genes were selected because of their reported roles in regulating IFN-I production,[48–52] which is dampened by saturated fatty acids. We found that *Nlrc3* was the only gene in this panel that was significantly upregulated in obese tumors (Figure 5A). To confirm this finding, we first stained the tumors grown in lean and obese mice with an anti-Nlrc3 antibody. We found that cancer cell-specific Nlrc3 expression was significantly elevated in the obese group (Figure 5B). Then, we also assessed the expression levels of *Nlrc3* in TAMs. We analyzed the single-cell dataset presented in Figure 2 and found that *Nlrc3* expression levels were significantly higher in the TAMs from tumors grown in obese hosts, including cluster 3 ($CD206^+Arg1^+$), cluster 7 ($PD\text{-}L1^+$), cluster 14 ($Cox2^+$), and cluster 17 ($Tgfb1^+$) (Figure 5C). These findings suggest that obesity upregulated the expression levels of Nlrc3 in both cancer cells and TAMs. Because the STING-suppressive role of NLRC3 in myeloid cells has been reported,[53] here we focus on whether NLRC3 senses saturated fatty acids and dampens IFN-I production in cancer cells. We performed reciprocal co-immunoprecipitation using HA-tagged NLRC3 and FLAG-tagged STING in PCI13, FaDu, and UMSCC22A cells. NLRC3 strongly interacted with STING in HNSCC cells under stringent buffer conditions (Figures 5D, 5E, and S4A), in agreement with previous findings in HEK-293T cells.[52] Then, we generated *NLRC3*-deficient human HNSCC cells using CRISPR-Cas9 lentiviruses. Due to frequent intrinsic inhibition of the STING-IFN-I pathway, we found that human HNSCC cells often fail to respond to the physiologic ligand of STING, CDNs.[5] Thus, we tested two additional approaches that can activate the STING pathway. We first transfected empty vector (EV) control and *NLRC3*-deficient PCI-13 cells with 1.0 μg/mL STING expression plasmid or 1.0 μg/mL poly(dA:dT) 16 h prior to RNA harvesting. We found that *NLRC3* loss led to significantly increased expression of the STING-mediated IFN-I gene signatures *ISG15*, *MX1*, and *ISG54* (Figures 5F–5H and S4B). Similarly, we used the same approach to repress NLRC3 expression in FaDu cells. A defect in *NLRC3* enhanced STING- and poly(dA:dT)-induced immune activation (Figures 5I–5K and S4B).

To model the impact of NLRC3 on HNSCC immunogenicity, we then knocked down *Nlrc3* in MOC2-E6/E7 cells, confirmed by qPCR and immunoblots (Figures 6A and 6B). An alamarBlue assay showed that there were no differences in growth rates between the EV- and *Nlrc3*-deficient tumor cells (Figure 6C). To substantiate the link between saturated fatty acids sensing and *Nlrc3*-mediated suppression of the STING pathway, we first treated MOC2-E6/E7 cells with either carrier BSA or 200 μM palmitate-BSA. We found that palmitate significantly increased the expression levels of *Nlrc3* (Figures 6D and 6E). Then, we transfected EV- and *Nlrc3*-deficient tumor cells with either 1.0 μg/mL STING expression plasmid or 1.0 μg/mL poly(dA:dT) for 16 h. *Nlrc3*-deficient cells exhibited significantly increased expression levels of *Ifnb1*, *Cxcl9*, *Cxcl10,* and *Mx1* from both STING-transfected samples (Figure 6F) as well as samples treated with poly(dA:dT) (Figure 6G). Last, we characterized the impact of Nlrc3 on STING signaling by immunoblots. We found that a defect in Nlrc3 resulted in much higher levels of the signaling hallmarks of STING activation, including the phospho-Tbk1 and phospho-Irf3, in response to either STING expression or poly(dA:dT) transfection (Figures 6H and 6I).

Nlrc3 inhibits HNSCC immunogenicity in an IFN-I-dependent fashion

To assess whether Nlrc3 regulates the immunogenicity of HNSCC, we first implanted one million EV- or shNlrc3-MOC2-E6/E7 cancer cells subcutaneously in normal C57BL/6 mice.

Figure 5. Saturated fatty acids induce the expression of *NLRC3* to antagonize STING signaling in human HNSCC cells

(A) Total RNA was isolated from whole excised tumors to quantify the mRNA expression levels of *Nlrp3*, *Nod2*, *Nlrp12*, *Nlrx1*, and *Nlrc3* (n = 8 normal-weight mice; n = 6 obese mice). Values represent mean ± SEM of three technical replicates per tumor. All comparisons between the two groups were made using a two-tailed unpaired *t* test (n.s. $p > 0.05$; *$p < 0.05$).

(B) Tumors from obese and lean mice were harvested for H&E and NLRC3 IHC staining. Representative H&E and IHC staining patterns are shown. NLRC3 staining intensity was quantitated using ImageJ. Scale bar, 200 μm. Values represent mean ± SEM of four representative staining per group. The comparison between the two groups was made using a two-tailed unpaired t test (*$p < 0.05$).

(C) The expression levels of *Nlrc3* (Log) in tumor-associated myeloid cells, including clusters 3, 7, 14, and 17, were compared between lean and obese mice. (*$p < 0.05$, ***$p < 0.001$, ****$p < 0.0001$).

(D and E) Human HNSCC cell lines PCI-13 and FaDu were transfected with 1.0 μg/mL human HA-NLRC3 and FLAG-STING plasmids. STING and NLRC3 proteins were pulled down using anti-FLAG M2 affinity gel and anti-HA agarose, respectively. Immunoblots were performed for the indicated proteins.

(F) PCI-13 cells were transduced with empty vector (EV) or *NLRC3*-targeted CRISPR-Cas9 lentiviruses. Stable cell lines were generated via puromycin selection. Immunoblots and qPCR were used to confirm the knockout efficiency. Comparison between the two groups was made using a two-tailed unpaired t test (*$p < 0.05$).

(G and H) EV and $NLRC3^{-/-}$ PCI-13 cells were transfected with either 1.0 μg/mL human STING expression plasmid (G) or 1.0 μg/mL poly(dA:dT) (H) for 16 h. The mRNA levels of human *ISG15* and *MX1* were assessed via qPCR. Values represent mean ± SEM of three biological replicates per sample.

(I and J) FaDu cells were transduced with EV or *NLRC3*-targeted CRISPR-Cas9 lentiviruses. Stable cell lines were generated via puromycin selection. Proteins and total RNA from cells were isolated and the knockout efficiency of *NLRC3* quantified via immunoblots and qPCR, respectively. EV and $NLRC3^{-/-}$ FaDu cells were transfected with either 1.0 μg/mL human STING expression plasmid (J) or 1.0 μg/mL poly(dA:dT) (K) for 16 h. The expression levels of human *ISG15* and *MX1* were assessed via qPCR. Values represent mean ± SEM of three biological replicates per sample. Data represent two experiments. Comparisons were made using one-way ANOVA followed by multi-comparison tests (**$p < 0.01$; ****$p < 0.0001$).

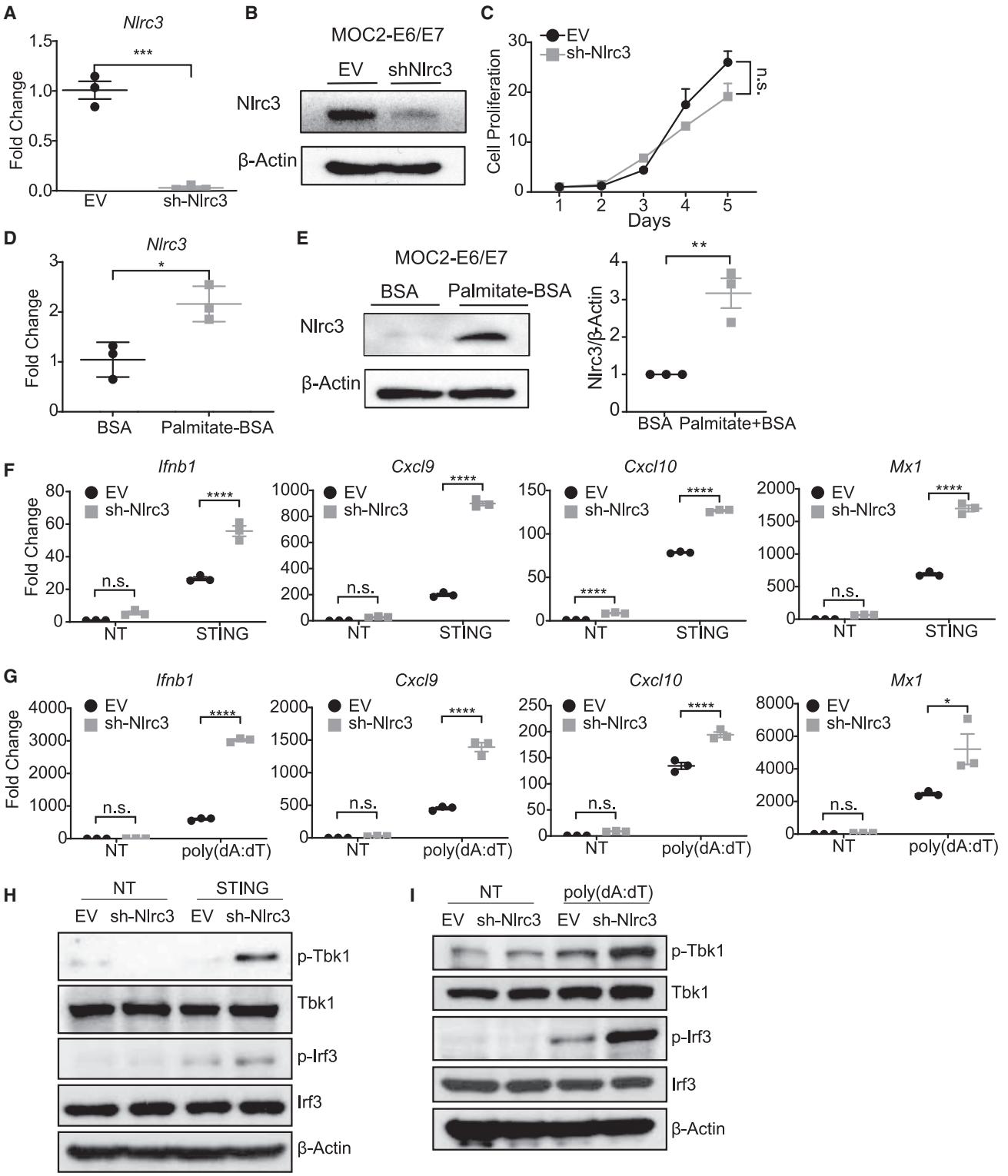

Figure 6. NLRC3 inhibits the STING-IFN-I pathway in murine HNSCC cells

(A and B) MOC2-E6/E7 was transduced with an empty vector (EV) or *Nlrc3*-targeting short hairpin RNA lentiviruses. Stable cell lines were generated via enhanced puromycin selection. Knockdown efficiency was confirmed via qPCR (A) and immunoblots (B). Comparisons between the two groups were made using a two-tailed unpaired t test (***$p < 0.001$).

(legend continued on next page)

We monitored tumor burden and found that a cancer-cell intrinsic loss of *Nlrc3* resulted in significantly delayed tumor growth (Figure 7A). To assess whether the observed tumor rejection in the *Nlrc3*-deficient tumors was immune-mediated, we implanted EV control and *Nlrc3*-deficient MOC2-E6/E7 cells into *Rag1*$^{-/-}$ mice, which were devoid of mature T cells and B cells. We found that the lack of adaptive immunity completely rescued the phenotype, with no differences found between the two groups (Figure 7B). Then, we implanted the control and *Nlrc3*-deficient tumors in *Ifnar1*$^{-/-}$ mice, which lacked the expression of the receptor for IFN-I. Similar to the *Rag1*$^{-/-}$ hosts, few differences in tumor burden were found between the two groups (Figure 7C). These experiments suggest that cancer-cell intrinsic Nlrc3-mediates HNSCC immunogenicity in an IFN-I-dependent fashion. Next, we homogenized tumor tissue from EV- and *Nlrc3*-deficient MOC2-E6/E7-bearing C57BL/6 mice and assessed for the expression levels of Th1 cytokines associated with T cell recruitment and activation. We found that the expression levels of *Cxcl9*, *Cxcl10*, *Tnf*, and *Ifng* were significantly enhanced in *Nlrc3*-deficient tumors (Figure 7D). We enriched TILs through Ficoll-Paque gradient centrifugation and found that cancer-cell intrinsic loss of *Nlrc3* resulted in the increased frequencies of overall T cells, γδ T cells, and CD8^{+}PD-1^{low} T cells, which we previously found to exhibit more robust effector functions (Figures 7E–7G).[37] As saturated fatty acids induced the expression of *Nlrc3* in cancer cells, serving as a possible link to suppress cancer immunogenicity, we next implanted *Nlrc3*-deficient tumor cells into mice that were fed with regular chow or a 60% kcal high-fat diet for twelve weeks. High-fat diet induced significant body weight gain, as expected (Figure S4C). The difference in tumor burden that we observed between lean and obese mice using wild-type tumor cells was completely rescued (Figures S4D and S4E), suggesting that cancer-specific *Nlrc3* expression is a key link underpinning obesity-potentiated suppression of HNSCC immunogenicity.

DISCUSSION

The discovery of checkpoints of the adaptive immune system revolutionized cancer therapy by improving the effector functions of intra-tumoral T cells. With the ICB therapies targeting T cells being brought up to the first-line setting, it has become clear that the majority of tumors feature suppression of the innate immune sensing system, which leads to an insufficient pool of intra-tumoral antigen-specific T cells for developing an optimal response. Thus, the identification of cancer checkpoints involving the innate immune sensing pathways is essential to designing new innate immune priming strategies and expanding the pool of responders to immunotherapy.

Recent studies have suggested that multiple priming approaches exacerbate tumor DNA damage and engage the STING-IFN-I pathway for the remodeling of TME. For example, the inhibitors of DNA damage repair activate the STING-IFN-I pathway and sensitize cold cancers to ICB.[54,55] External beam radiotherapy and targeted radionuclide therapy can also both activate STING-dependent IFN-I signaling to effectively prime cold cancers.[56] In fact, the efficacy of radiotherapy is largely lost in STING-deficient hosts.[13] An epigenetic remodeling agent targeting a histone H3 lysine 9 trimethylation demethylase, KDM4A, sensitizes cold HNSCC to ICB by inducing replication stress-induced STING activation.[57] In addition, cancer-specific expression of STING is positively associated with patient outcomes in two independent clinical cohorts of HNSCC.[5] Thus, the maintenance of cancer cell "STING fitness" underpins the immunogenicity of HNSCC.

Although oncogene-driven suppression of the STING-IFN-I pathway has been identified, it remains unclear whether metabolic comorbidities contribute to the editing of cancer immunogenicity. Multiple large independent prospective cohorts have recently presented an underappreciated link between obesity and the development of HNSCC,[16–19] which entails the establishment of peripheral immune tolerance. To better understand the molecular mechanism linking obesity to reduced HNSCC immunogenicity, this study characterized a signaling axis that pinpointed NLRC3, an innate immune checkpoint NLR protein, serving as a saturated fatty acids responder. Saturated fatty acids, but not unsaturated fatty acids, potently inhibit STING-mediated immune activation. Many cancer cells, including HNSCC, show defective STING signaling and do not mount an IFN-I response upon CDN challenge.[6,58] We, therefore, used STING plasmid expression as one of the stimuli. Even with this strong STING stimulation, palmitate, but not oleate, nearly abrogated immune activation. NLRC3 undergoes adaptive upregulation in response to palmitate and negatively impacts HNSCC immunogenicity. *NLRC3*-deficient tumors were rejected by the adaptive immune system in an IFN-I-dependent fashion. NLRC3 binds to cytoplasmic DNA species, releasing its interaction with STING and licensing the downstream IFN-I generation process.[52,53]

Obesity creates an IFN-I-deprived TME, which drives *de novo* development and influx of MDSCs to HNSCC. We characterized the impact of obesity on TME at single-cell resolution and

(C) The proliferation of EV control and sh-Nlrc3-MOC2-E6/E7 cells was assessed using an alamarBlue assay. Each group included five replicate wells. Comparisons at endpoint were made using a two-tailed unpaired t test (n.s. $p > 0.05$).

(D and E) *Nlrc3* expression was measured in MOC2-E6/E7 cells treated with either BSA alone or 200 μM palmitate-BSA for 24 h via qPCR (D) and immunoblots (E). Densitometry analysis was performed using ImageJ and is shown in the right panel (E). Comparisons between two groups were made using a two-tailed unpaired t test (*$p < 0.05$, *$p < 0.01$).

(F and G) EV- and sh-Nlrc3-MOC2-E6/E7 cells were transfected with either (F) 1.0 μg/mL Sting expression plasmid or (G) 1.0 μg/mL poly(dA:dT) for 16 h. Total RNA from cells was isolated. Expression of murine *Ifnb1*, pan-*Ifnα*, *Cxcl9*, *Cxcl10*, and *Mx1* was assessed via qPCR. Values represent mean ± SEM of three biological replicates per sample. Experiments were performed twice. Comparisons were made using one-way ANOVA followed by multi-comparison tests (*$p < 0.05$; ****$p < 0.0001$).

(H and I) EV- and sh-Nlrc3-MOC2-E6/E7 cells were transfected with either 1.0 μg/mL mouse Sting expression plasmid (H) or 1.0 μg/mL poly(dA:dT) (I) for 16 h. Cell lysates were subjected to SDS-PAGE for the indicated markers.

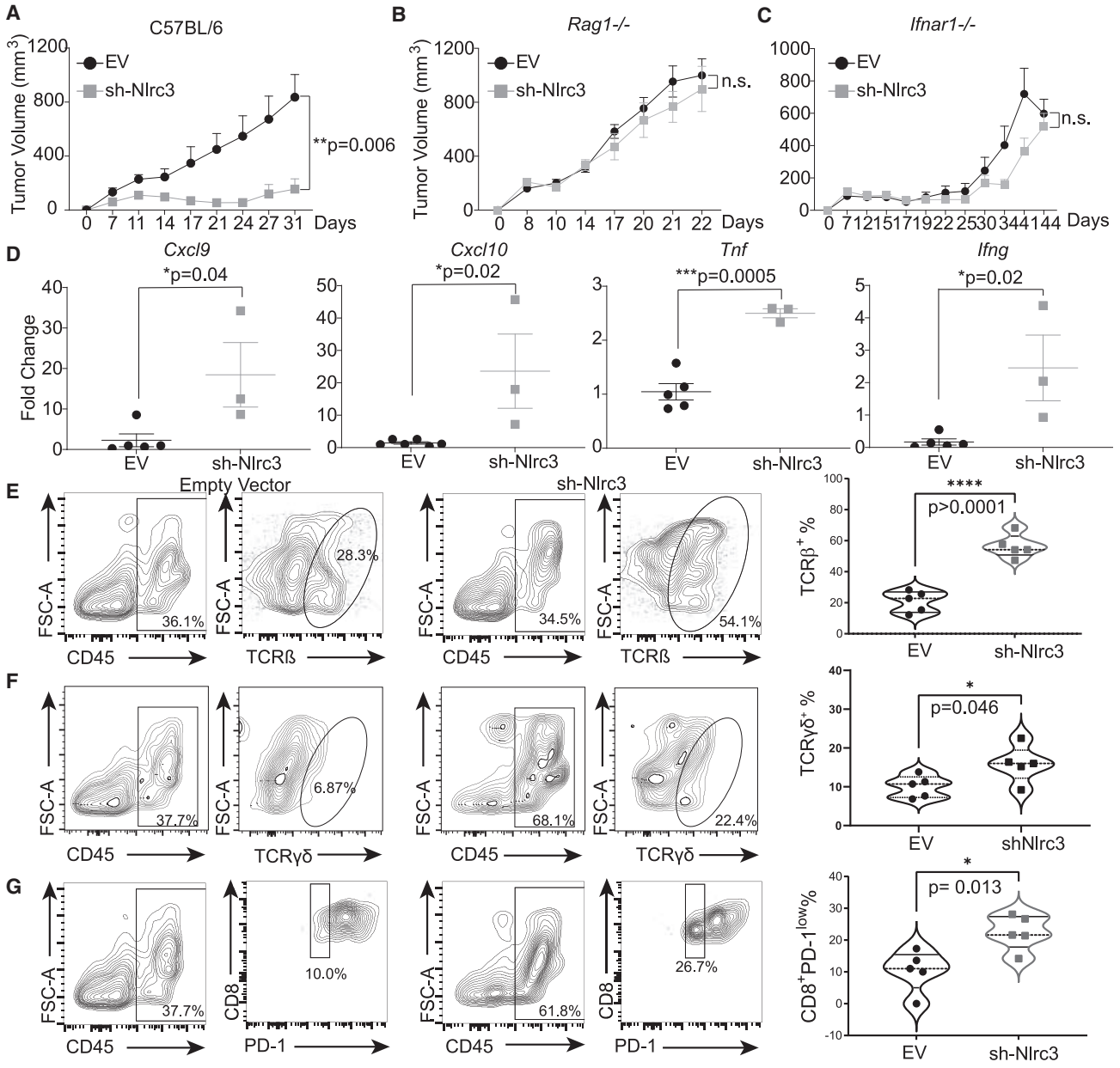

Figure 7. NLRC3 inhibits HNSCC immunogenicity in an IFN-I-dependent fashion

(A) One million EV- or sh-Nlrc3-MOC2-E6/E7 cancer cells were implanted subcutaneously (s.c.) into the right flank of 13-week-old C57BL/6 mice and monitored for tumor burden (n = 5 mice per group). Tumor measurements occurred every 2–4 days. Experiments were conducted twice. Differences between groups were assessed using the generalized estimating equation model (**$p < 0.01$).

(B) One million EV- or sh-Nlrc3-MOC2-E6/E7 cancer cells were implanted s.c. into the right flank of six-week-old *Rag1*$^{-/-}$ mice and monitored for tumor burden (n = 5 per group). Tumor measurements occurred every 2–4 days.

(C) One million EV- or sh-Nlrc3-MOC2-E6/E7 cancer cells were implanted s.c. into the right flank of six-week-old *Ifnar1*$^{-/-}$ mice that were backcrossed to C57BL/6J for over nine generations and monitored for tumor burden (n = 7 per group). Differences between groups were assessed using the generalized estimating equation model (n.s. $p > 0.05$).

(D) Total RNA was isolated from one representative set of whole excised tumors and quantified for the mRNA expression levels of *Cxcl9*, *Cxcl10*, *Tnf*, and *Ifng* (n = 5 mice with EV-MOC2-E6/E7 tumors; n = 3 mice with sh-Nlrc3-MOC2-E6/E7 tumors due to complete tumor regression). Values represent mean ± SEM of three technical replicates per tumor. All comparisons between two groups were made using a two-tailed unpaired t test (*$p < 0.05$; ***$p < 0.001$).

(E–G) TILs from one representative set of experiments were isolated and analyzed by flow cytometry. The gating strategy for all experiments was as follows: Lymphocytes, single cells, Zombie Aqua negative (viability), CD45^{+} (n = 5 mice per condition). Comparisons between two groups were made using a two-tailed unpaired t test (*$p < 0.05$, ****$p < 0.0001$).

revealed a massive expansion of suppressive myeloid cell clusters in the TILs from obese hosts. These myeloid clusters assume diverse complementary features. Only a subset of these suppressive myeloid cells expresses PD-L1 or Galectin-9. Other suppressive cells feature high expression levels of *Tgfb1*, *Arg1*, or *Cox2*. TILs from obese hosts showed more $Cox2^+$ MDSCs, more $CD206^+Arg1^+$ myeloid cells, and fewer $STING^+$ myeloid cells. As a result, effector T cells within the TME of obese hosts are both fewer and less functional. STING agonists have been evaluated for their potency in reducing tumor burden by reprogramming the myeloid compartment in a variety of tumor models.[59] Myeloid cells are generally considered to be the main target of intra-tumoral CDN injections. Notably, our findings show that not all myeloid cells will respond to CDNs. BMDMs and peritoneal macrophages separated from the obese hosts are largely refractory to STING agonists. The MDSCs from obese mice are also more suppressive. In agreement, intra-tumoral injection of a potent stable STING agonist lost efficacy in obese mice. Interestingly, obesity-mediated reprogramming of myeloid cells appears to be specific to the STING pathway because these cells retain their sensitivity to RIG-I agonists. To further corroborate the mechanistic link between obesity and NLRC3-mediated STING suppression, we found that NLRC3-deficiency rescued the tumor growth difference between lean and obese hosts. As many priming strategies rely on the STING pathway, future studies would be informative to assess strategies to overcome obesity-induced desensitization to STING priming.

Limitations of the study

The clinical data on the impact of obesity on HNSCC response to ICBs are still limited. Several considerations in clinical study design may help better characterize the impact of common metabolic comorbidity on tumor immunogenicity. First, many HNSCC patients show bodyweight fluctuations around the time of diagnosis due to cancer or associated habits. Many HNSCCs directly interfere with eating and swallowing. Thus, initial characterization using early-stage tumors may reduce the number of confounding factors. Indeed, among patients with T1-T2 HNSCC who underwent curative-intent resection, obesity was a significant negative prognosticator and obesity-associated white adipose tissue inflammation was associated with worse outcomes.[60,61] Second, body mass index, although easily accessible, may not be the most accurate measurement for obesity. For example, trained athletes can have substantially increased body mass index yet are not obese. Thus, other measurements such as waist circumference, waist-to-hip ratio, and a peripheral blood lipid panel, may be assessed in the design. Last but not least, the medication history of statins should be considered. Recent findings show that inhibiting the cholesterol biosynthetic pathway activates the STING-IFN-I pathway.[62] Conceptually in agreement, lipophilic statins show notable vaccine adjuvant effects and anti-tumor potency.[63] HPV^+ HNSCC patients who were on statins also showed improved clinical outcomes.[20,21]

In this study, we emphasized the role of NLRC3 in underpinning obesity-associated desensitization of cells to STING agonists. However, the high-fat diet model and *in vitro* treatments with saturated fatty acids modulate multiple pathways, such as endoplasmic reticulum stress and insulin signaling. It would be helpful to assess additional molecular pathways that link obesity with IFN-I response. We focused on the cancer cell-specific role of NLRC3 in driving tumor immune escape. It is also possible that NLRC3 expression in host cells also contributes to obesity-mediated tumor immunogenicity. Additional studies to examine the function of NLRC3 in different immune subsets using tumor models with obesity being a comorbidity will help further delineate the compartment-specific roles of NLRC3.

Overall, this study rendered a single-cell immune atlas for HNSCC growing in a high-fat environment and linked saturated fatty acids with DNA-binding, STING-inhibitory, innate immune checkpoint, NLRC3. Saturated fatty acids, but not unsaturated fatty acids, potently inhibited STING activation in both cancer cells and myeloid cells. Both BMDMs and peritoneal macrophages in obese hosts were desensitized to STING stimulation. MDSCs from obese hosts were also more suppressive of T cell activation. We found that cancer-cell intrinsic NLRC3 expression was a central regulator of HNSCC immunogenicity. Depletion of NLRC3 resulted in IFN-I-dependent tumor rejection and rescued the NLRC3-wild-type tumor growth difference between lean and obese mice. These results provide a mechanistic link between obesity and elevated risks for HNSCC.

STAR★METHODS

Detailed methods are provided in the online version of this paper and include the following:

- KEY RESOURCES TABLE
- RESOURCE AVAILABILITY
  - Lead contact
  - Materials availability
  - Data and code availability
- EXPERIMENTAL MODEL AND SUBJECT DETAILS
  - Animal studies
  - Cell lines and treatments
  - Bone marrow-derived macrophages (BMDMs) isolation and differentiation
  - Peritoneal macrophages isolation and differentiation
- METHOD DETAILS
  - Preparation of fatty acid conjugates
  - Gene expression qPCR & ELISA
  - Immunoblotting assays
  - Histology, immunohistochemistry, and oil red O staining
  - AlamarBlue assay
  - Quantitation of serum cholesterol levels
  - Flow cytometry
  - MDSC functional assay
  - Single-cell immune profiling
- QUANTIFICATION AND STATISTICAL ANALYSIS

SUPPLEMENTAL INFORMATION

Supplemental information can be found online at https://doi.org/10.1016/j.celrep.2023.112303.

ACKNOWLEDGMENTS

The FLAG-STING expression plasmid was kindly provided by Dr. Glen N. Barber at the University of Miami. The HA-NLRC3 expression plasmid was a generous gift from Dr. Jenny P.-Y. Ting at the University of North Carolina at Chapel Hill. This research was funded by NIH grants R01 DE026728, R01 DE030691, R01 DE031951, U01 DE029255, F31 DE028740, and T32 AI007413. The core facilities are supported, in part, by P30 CA046592.

AUTHOR CONTRIBUTIONS

B.R.H., W.G., H.F.T., L.B., K.O., W.C., M.J., and Z.R.F. performed experiments and contributed to data acquisition. A.M., W.S., and Y.X. advised on statistical analysis and performed data analyses. Y.X., A.M., and Y.L.L. analyzed the single-cell dataset. B.R.H., W.G., H.F.T., J.J.M., and Y.L.L. designed the project with significant intellectual input from S.B.C., S.Z., H.W., and J.J.M. Y.X., H.W., and E.B. provided key resources and technical support. B.R.H., W.G., H.F.T., and Y.L.L. wrote the manuscript, and all authors edited the manuscript and have read and agreed to its contents.

DECLARATION OF INTERESTS

J.J.M. and Y.L.L. are co-founders and serve on the advisory board of Saros Inc. Y.L.L. is on the scientific advisory board of Brooklyn Immunotherapeutics. All authors do not have patents related to this study. The funders had no role in the design of the study; in the collection, analyses, or interpretation of data; in the writing of the manuscript; or in the decision to publish the results.

INCLUSION AND DIVERSITY

We support inclusive, diverse, and equitable conduct of research. One or more of the authors of this paper self-identifies as an underrepresented ethnic minority in their field of research or within their geographical location. One or more of the authors of this paper self-identifies as a gender minority in their field of research.

Received: November 10, 2021
Revised: December 21, 2022
Accepted: March 6, 2023

REFERENCES

1. Henley, S.J., Ward, E.M., Scott, S., Ma, J., Anderson, R.N., Firth, A.U., Thomas, C.C., Islami, F., Weir, H.K., Lewis, D.R., et al. (2020). Annual report to the nation on the status of cancer, part I: national cancer statistics. Cancer *126*, 2225–2249. https://doi.org/10.1002/cncr.32802.
2. Gillison, M.L., Chaturvedi, A.K., Anderson, W.F., and Fakhry, C. (2015). Epidemiology of human papillomavirus-positive head and neck squamous cell carcinoma. J. Clin. Oncol. *33*, 3235–3242. https://doi.org/10.1200/JCO.2015.61.6995.
3. Cohen, E.E.W., Soulières, D., Le Tourneau, C., Dinis, J., Licitra, L., Ahn, M.J., Soria, A., Machiels, J.P., Mach, N., Mehra, R., et al. (2019). Pembrolizumab versus methotrexate, docetaxel, or cetuximab for recurrent or metastatic head-and-neck squamous cell carcinoma (KEYNOTE-040): a randomised, open-label, phase 3 study. Lancet *393*, 156–167. https://doi.org/10.1016/S0140-6736(18)31999-8.
4. Ferris, R.L., Blumenschein, G., Jr., Fayette, J., Guigay, J., Colevas, A.D., Licitra, L., Harrington, K., Kasper, S., Vokes, E.E., Even, C., et al. (2016). Nivolumab for recurrent squamous-cell carcinoma of the head and neck. N. Engl. J. Med. *375*, 1856–1867. https://doi.org/10.1056/NEJMoa1602252.
5. Luo, X., Donnelly, C.R., Gong, W., Heath, B.R., Hao, Y., Donnelly, L.A., Moghbeli, T., Tan, Y.S., Lin, X., Bellile, E., et al. (2020). HPV16 drives cancer immune escape via NLRX1-mediated degradation of STING. J. Clin. Invest. *130*, 1635–1652. https://doi.org/10.1172/JCI129497.
6. Tan, Y.S., Sansanaphongpricha, K., Xie, Y., Donnelly, C.R., Luo, X., Heath, B.R., Zhao, X., Bellile, E., Hu, H., Chen, H., et al. (2018). Mitigating SOX2-potentiated immune escape of head and neck squamous cell carcinoma with a STING-inducing nanosatellite vaccine. Clin. Cancer Res. *24*, 4242–4255. https://doi.org/10.1158/1078-0432.CCR-17-2807.
7. Wang, X., Schoenhals, J.E., Li, A., Valdecanas, D.R., Ye, H., Zang, F., Tang, C., Tang, M., Liu, C.G., Liu, X., et al. (2017). Suppression of type I IFN signaling in tumors mediates resistance to anti-PD-1 treatment that can Be overcome by radiotherapy. Cancer Res. *77*, 839–850. https://doi.org/10.1158/0008-5472.CAN-15-3142.
8. Zebertavage, L.K., Alice, A., Crittenden, M.R., and Gough, M.J. (2020). Transcriptional upregulation of NLRC5 by radiation drives STING- and interferon-independent MHC-I expression on cancer cells and T cell cytotoxicity. Sci. Rep. *10*, 7376. https://doi.org/10.1038/s41598-020-64408-3.
9. Pieper, A.A., Rakhmilevich, A.L., Spiegelman, D.V., Patel, R.B., Birstler, J., Jin, W.J., Carlson, P.M., Charych, D.H., Hank, J.A., Erbe, A.K., et al. (2021). Combination of radiation therapy, bempegaldesleukin, and checkpoint blockade eradicates advanced solid tumors and metastases in mice. J. Immunother. Cancer *9*, e002715. https://doi.org/10.1136/jitc-2021-002715.
10. Leidner, R., Crittenden, M., Young, K., Xiao, H., Wu, Y., Couey, M.A., Patel, A.A., Cheng, A.C., Watters, A.L., Bifulco, C., et al. (2021). Neoadjuvant immunoradiotherapy results in high rate of complete pathological response and clinical to pathological downstaging in locally advanced head and neck squamous cell carcinoma. J. Immunother. Cancer *9*, e002485. https://doi.org/10.1136/jitc-2021-002485.
11. Jagodinsky, J.C., Jin, W.J., Bates, A.M., Hernandez, R., Grudzinski, J.J., Marsh, I.R., Chakravarty, I., Arthur, I.S., Zangl, L.M., Brown, R.J., et al. (2021). Temporal analysis of type 1 interferon activation in tumor cells following external beam radiotherapy or targeted radionuclide therapy. Theranostics *11*, 6120–6137. https://doi.org/10.7150/thno.54881.
12. Burnette, B.C., Liang, H., Lee, Y., Chlewicki, L., Khodarev, N.N., Weichselbaum, R.R., Fu, Y.X., and Auh, S.L. (2011). The efficacy of radiotherapy relies upon induction of type i interferon-dependent innate and adaptive immunity. Cancer Res. *71*, 2488–2496. https://doi.org/10.1158/0008-5472.CAN-10-2820.
13. Deng, L., Liang, H., Xu, M., Yang, X., Burnette, B., Arina, A., Li, X.D., Mauceri, H., Beckett, M., Darga, T., et al. (2014). STING-dependent cytosolic DNA sensing promotes radiation-induced type I interferon-dependent antitumor immunity in immunogenic tumors. Immunity *41*, 843–852. https://doi.org/10.1016/j.immuni.2014.10.019.
14. Knitz, M.W., Bickett, T.E., Darragh, L.B., Oweida, A.J., Bhatia, S., Van Court, B., Bhuvane, S., Piper, M., Gadwa, J., Mueller, A.C., et al. (2021). Targeting resistance to radiation-immunotherapy in cold HNSCCs by modulating the Treg-dendritic cell axis. J. Immunother. Cancer *9*, e001955. https://doi.org/10.1136/jitc-2020-001955.
15. Saloura, V., Fatima, A., Zewde, M., Kiyotani, K., Brisson, R., Park, J.H., Ikeda, Y., Vougiouklakis, T., Bao, R., Khattri, A., et al. (2017). Characterization of the T-cell receptor repertoire and immune microenvironment in patients with locoregionally advanced squamous cell carcinoma of the head and neck. Clin. Cancer Res. *23*, 4897–4907. https://doi.org/10.1158/1078-0432.CCR-17-0103.
16. Etemadi, A., O'Doherty, M.G., Freedman, N.D., Hollenbeck, A.R., Dawsey, S.M., and Abnet, C.C. (2014). A prospective cohort study of body size and risk of head and neck cancers in the NIH-AARP diet and health study. Cancer Epidemiol. Biomarkers Prev. *23*, 2422–2429. https://doi.org/10.1158/1055-9965.Epi-14-0709-t.
17. Recalde, M., Davila-Batista, V., Díaz, Y., Leitzmann, M., Romieu, I., Freisling, H., and Duarte-Salles, T. (2021). Body mass index and waist circumference in relation to the risk of 26 types of cancer: a prospective cohort study of 3.5 million adults in Spain. BMC Med. *19*, 10. https://doi.org/10.1186/s12916-020-01877-3.
18. Kim, H.B., Kim, G.J., Han, K.D., and Joo, Y.H. (2021). Changes in metabolic syndrome status and risk of laryngeal cancer: a nationwide cohort

study. PLoS One *16*, e0252872. https://doi.org/10.1371/journal.pone.0252872.

19. Khanna, A., Sturgis, E.M., Dahlstrom, K.R., Xu, L., Wei, Q., Li, G., and Gross, N.D. (2021). Association of pretreatment body mass index with risk of head and neck cancer: a large single-center study. Am. J. Cancer Res. *11*, 2343–2350.
20. Gupta, A., Stokes, W., Eguchi, M., Hararah, M., Amini, A., Mueller, A., Morgan, R., Bradley, C., Raben, D., McDermott, J., and Karam, S.D. (2019). Statin use associated with improved overall and cancer specific survival in patients with head and neck cancer. Oral Oncol. *90*, 54–66. https://doi.org/10.1016/j.oraloncology.2019.01.019.
21. Getz, K.R., Bellile, E., Zarins, K.R., Rullman, C., Chinn, S.B., Taylor, J.M.G., Rozek, L.S., Wolf, G.T., and Mondul, A.M. (2020). Statin use and head and neck squamous cell carcinoma outcomes. Int. J. Cancer. https://doi.org/10.1002/ijc.33441.
22. Moore, E., Clavijo, P.E., Davis, R., Cash, H., Van Waes, C., Kim, Y., and Allen, C. (2016). Established T cell-inflamed tumors rejected after adaptive resistance was reversed by combination STING activation and PD-1 pathway blockade. Cancer Immunol. Res. *4*, 1061–1071. https://doi.org/10.1158/2326-6066.CIR-16-0104.
23. Fu, J., Kanne, D.B., Leong, M., Glickman, L.H., McWhirter, S.M., Lemmens, E., Mechette, K., Leong, J.J., Lauer, P., Liu, W., et al. (2015). STING agonist formulated cancer vaccines can cure established tumors resistant to PD-1 blockade. Sci. Transl. Med. *7*, 283ra52. https://doi.org/10.1126/scitranslmed.aaa4306.
24. Sun, X., Zhang, Y., Li, J., Park, K.S., Han, K., Zhou, X., Xu, Y., Nam, J., Xu, J., Shi, X., et al. (2021). Amplifying STING activation by cyclic dinucleotide-manganese particles for local and systemic cancer metalloimmunotherapy. Nat. Nanotechnol. *16*, 1260–1270. https://doi.org/10.1038/s41565-021-00962-9.
25. Lang, P., Hasselwander, S., Li, H., and Xia, N. (2019). Effects of different diets used in diet-induced obesity models on insulin resistance and vascular dysfunction in C57BL/6 mice. Sci. Rep. *9*, 19556. https://doi.org/10.1038/s41598-019-55987-x.
26. Le, Q.-T., Courter, D., and Giaccia, A. (2010). Hypoxia, angiogenesis, and oral cancer metastasis. In Oral Cancer Metastasis, J.N. Myers, ed. (Springer), pp. 302–304. https://doi.org/10.1007/978-1-4419-0775-2.
27. Zhang, H., Bosch-Marce, M., Shimoda, L.A., Tan, Y.S., Baek, J.H., Wesley, J.B., Gonzalez, F.J., and Semenza, G.L. (2008). Mitochondrial autophagy is an HIF-1-dependent adaptive metabolic response to hypoxia. J. Biol. Chem. *283*, 10892–10903. https://doi.org/10.1074/jbc.M800102200.
28. Levine, B., and Kroemer, G. (2008). Autophagy in the pathogenesis of disease. Cell *132*, 27–42. https://doi.org/10.1016/j.cell.2007.12.018.
29. Liu, Y., Shoji-Kawata, S., Sumpter, R.M., Jr., Wei, Y., Ginet, V., Zhang, L., Posner, B., Tran, K.A., Green, D.R., Xavier, R.J., et al. (2013). Autosis is a Na+,K+-ATPase-regulated form of cell death triggered by autophagy-inducing peptides, starvation, and hypoxia-ischemia. Proc. Natl. Acad. Sci. USA *110*, 20364–20371. https://doi.org/10.1073/pnas.1319661110.
30. Wan, G., Xie, W., Liu, Z., Xu, W., Lao, Y., Huang, N., Cui, K., Liao, M., He, J., Jiang, Y., et al. (2014). Hypoxia-induced MIR155 is a potent autophagy inducer by targeting multiple players in the MTOR pathway. Autophagy *10*, 70–79. https://doi.org/10.4161/auto.26534.
31. Sugiura, A., and Rathmell, J.C. (2018). Metabolic barriers to T cell function in tumors. J. Immunol. *200*, 400–407. https://doi.org/10.4049/jimmunol.1701041.
32. Siska, P.J., and Rathmell, J.C. (2015). T cell metabolic fitness in antitumor immunity. Trends Immunol. *36*, 257–264. https://doi.org/10.1016/j.it.2015.02.007.
33. Delgoffe, G.M., and Powell, J.D. (2015). Feeding an army: the metabolism of T cells in activation, anergy, and exhaustion. Mol. Immunol. *68*, 492–496. https://doi.org/10.1016/j.molimm.2015.07.026.
34. Topalian, S.L., Taube, J.M., Anders, R.A., and Pardoll, D.M. (2016). Mechanism-driven biomarkers to guide immune checkpoint blockade in cancer therapy. Nat. Rev. Cancer *16*, 275–287. https://doi.org/10.1038/nrc.2016.36.
35. Palucka, A.K., and Coussens, L.M. (2016). The basis of oncoimmunology. Cell *164*, 1233–1247. https://doi.org/10.1016/j.cell.2016.01.049.
36. Li, J., Jie, H.B., Lei, Y., Gildener-Leapman, N., Trivedi, S., Green, T., Kane, L.P., and Ferris, R.L. (2015). PD-1/SHP-2 inhibits Tc1/Th1 phenotypic responses and the activation of T cells in the tumor microenvironment. Cancer Res. *75*, 508–518. https://doi.org/10.1158/0008-5472.CAN-14-1215.
37. Kansy, B.A., Concha-Benavente, F., Srivastava, R.M., Jie, H.B., Shayan, G., Lei, Y., Moskovitz, J., Moy, J., Li, J., Brandau, S., et al. (2017). PD-1 status in CD8(+) T cells associates with survival and anti-PD-1 therapeutic outcomes in head and neck cancer. Cancer Res. *77*, 6353–6364. https://doi.org/10.1158/0008-5472.CAN-16-3167.
38. Ahmad, R., Al-Roub, A., Kochumon, S., Akther, N., Thomas, R., Kumari, M., Koshy, M.S., Tiss, A., Hannun, Y.A., Tuomilehto, J., et al. (2018). The Synergy between palmitate and TNF-α for CCL2 production is dependent on the TRIF/IRF3 pathway: implications for metabolic inflammation. J. Immunol. *200*, 3599–3611. https://doi.org/10.4049/jimmunol.1701552.
39. Mayer, C.M., and Belsham, D.D. (2010). Palmitate attenuates insulin signaling and induces endoplasmic reticulum stress and apoptosis in hypothalamic neurons: rescue of resistance and apoptosis through adenosine 5′ monophosphate-activated protein kinase activation. Endocrinology *151*, 576–585. https://doi.org/10.1210/en.2009-1122.
40. Pascual, G., Avgustinova, A., Mejetta, S., Martín, M., Castellanos, A., Attolini, C.S.O., Berenguer, A., Prats, N., Toll, A., Hueto, J.A., et al. (2017). Targeting metastasis-initiating cells through the fatty acid receptor CD36. Nature *541*, 41–45. https://doi.org/10.1038/nature20791.
41. Boland, L.K., Burand, A.J., Boyt, D.T., Dobroski, H., Di, L., Liszewski, J.N., Schrodt, M.V., Frazer, M.K., Santillan, D.A., and Ankrum, J.A. (2019). Nature vs. Nurture: defining the effects of mesenchymal stromal cell isolation and culture conditions on resiliency to palmitate challenge. Front. Immunol. *10*, 1080. https://doi.org/10.3389/fimmu.2019.01080.
42. Li, L., Yin, Q., Kuss, P., Maliga, Z., Millán, J.L., Wu, H., and Mitchison, T.J. (2014). Hydrolysis of 2'3'-cGAMP by ENPP1 and design of nonhydrolyzable analogs. Nat. Chem. Biol. *10*, 1043–1048. https://doi.org/10.1038/nchembio.1661.
43. Casimiro, I., Stull, N.D., Tersey, S.A., and Mirmira, R.G. (2021). Phenotypic sexual dimorphism in response to dietary fat manipulation in C57BL/6J mice. J. Diabetes Complications *35*, 107795. https://doi.org/10.1016/j.jdiacomp.2020.107795.
44. Eckert, I., Ribechini, E., and Lutz, M.B. (2021). In vitro generation of murine myeloid-derived suppressor cells, analysis of markers, developmental commitment, and function. Methods Mol. Biol. *2236*, 99–114. https://doi.org/10.1007/978-1-0716-1060-2_10.
45. Swanson, K.V., Deng, M., and Ting, J.P.Y. (2019). The NLRP3 inflammasome: molecular activation and regulation to therapeutics. Nat. Rev. Immunol. *19*, 477–489. https://doi.org/10.1038/s41577-019-0165-0.
46. Costford, S.R., Tattoli, I., Duan, F.T., Volchuk, A., Klip, A., Philpott, D.J., Woo, M., and Girardin, S.E. (2018). Male mice lacking NLRX1 are partially protected from high-fat diet-induced hyperglycemia. J. Endocr. Soc. *2*, 336–347. https://doi.org/10.1210/js.2017-00360.
47. Motta, V., Soares, F., Sun, T., and Philpott, D.J. (2015). NOD-like receptors: versatile cytosolic sentinels. Physiol. Rev. *95*, 149–178. https://doi.org/10.1152/physrev.00009.2014.
48. Zheng, M., and Kanneganti, T.D. (2020). The regulation of the ZBP1-NLRP3 inflammasome and its implications in pyroptosis, apoptosis, and necroptosis (PANoptosis). Immunol. Rev. *297*, 26–38. https://doi.org/10.1111/imr.12909.
49. Lupfer, C., Thomas, P.G., and Kanneganti, T.D. (2014). Nucleotide oligomerization and binding domain 2-dependent dendritic cell activation is necessary for innate immunity and optimal CD8+ T Cell responses to

influenza A virus infection. J. Virol. *88*, 8946–8955. https://doi.org/10.1128/JVI.01110-14.

50. Chen, S.T., Chen, L., Lin, D.S.C., Chen, S.Y., Tsao, Y.P., Guo, H., Li, F.J., Tseng, W.T., Tam, J.W., Chao, C.W., et al. (2019). NLRP12 regulates antiviral RIG-I activation via interaction with TRIM25. Cell Host Microbe *25*, 602–616.e7. https://doi.org/10.1016/j.chom.2019.02.013.
51. Lei, Y., Wen, H., Yu, Y., Taxman, D.J., Zhang, L., Widman, D.G., Swanson, K.V., Wen, K.W., Damania, B., Moore, C.B., et al. (2012). The mitochondrial proteins NLRX1 and TUFM form a complex that regulates type I interferon and autophagy. Immunity *36*, 933–946. https://doi.org/10.1016/j.immuni.2012.03.025.
52. Zhang, L., Mo, J., Swanson, K.V., Wen, H., Petrucelli, A., Gregory, S.M., Zhang, Z., Schneider, M., Jiang, Y., Fitzgerald, K.A., et al. (2014). NLRC3, a member of the NLR family of proteins, is a negative regulator of innate immune signaling induced by the DNA sensor STING. Immunity *40*, 329–341. https://doi.org/10.1016/j.immuni.2014.01.010.
53. Li, X., Deng, M., Petrucelli, A.S., Zhu, C., Mo, J., Zhang, L., Tam, J.W., Ariel, P., Zhao, B., Zhang, S., et al. (2019). Viral DNA binding to NLRC3, an inhibitory nucleic acid sensor, unleashes STING, a cyclic dinucleotide receptor that activates type I interferon. Immunity *50*, 591–599.e6. https://doi.org/10.1016/j.immuni.2019.02.009.
54. Chabanon, R.M., Muirhead, G., Krastev, D.B., Adam, J., Morel, D., Garrido, M., Lamb, A., Hénon, C., Dorvault, N., Rouanne, M., et al. (2019). PARP inhibition enhances tumor cell-intrinsic immunity in ERCC1-deficient non-small cell lung cancer. J. Clin. Invest. *129*, 1211–1228. https://doi.org/10.1172/JCI123319.
55. Zhang, Q., Green, M.D., Lang, X., Lazarus, J., Parsels, J.D., Wei, S., Parsels, L.A., Shi, J., Ramnath, N., Wahl, D.R., et al. (2019). Inhibition of ATM increases interferon signaling and sensitizes pancreatic cancer to immune checkpoint blockade therapy. Cancer Res. *79*, 3940–3951. https://doi.org/10.1158/0008-5472.CAN-19-0761.
56. Patel, R.B., Hernandez, R., Carlson, P., Grudzinski, J., Bates, A.M., Jagodinsky, J.C., Erbe, A., Marsh, I.R., Arthur, I., Aluicio-Sarduy, E., et al. (2021). Low-dose targeted radionuclide therapy renders immunologically cold tumors responsive to immune checkpoint blockade. Sci. Transl. Med. *13*, eabb3631. https://doi.org/10.1126/scitranslmed.abb3631.
57. Zhang, W., Liu, W., Jia, L., Chen, D., Chang, I., Lake, M., Bentolila, L.A., and Wang, C.Y. (2021). Targeting KDM4A epigenetically activates tumor-cell-intrinsic immunity by inducing DNA replication stress. Mol. Cell *81*, 2148–2165.e9. https://doi.org/10.1016/j.molcel.2021.02.038.
58. Xia, T., Konno, H., Ahn, J., and Barber, G.N. (2016). Deregulation of STING signaling in colorectal carcinoma constrains DNA damage responses and correlates with tumorigenesis. Cell Rep. *14*, 282–297. https://doi.org/10.1016/j.celrep.2015.12.029.
59. Corrales, L., McWhirter, S.M., Dubensky, T.W., Jr., and Gajewski, T.F. (2016). The host STING pathway at the interface of cancer and immunity. J. Clin. Invest. *126*, 2404–2411. https://doi.org/10.1172/JCI86892.
60. Iyengar, N.M., Kochhar, A., Morris, P.G., Morris, L.G., Zhou, X.K., Ghossein, R.A., Pino, A., Fury, M.G., Pfister, D.G., Patel, S.G., et al. (2014). Impact of obesity on the survival of patients with early-stage squamous cell carcinoma of the oral tongue. Cancer *120*, 983–991. https://doi.org/10.1002/cncr.28532.
61. Iyengar, N.M., Ghossein, R.A., Morris, L.G., Zhou, X.K., Kochhar, A., Morris, P.G., Pfister, D.G., Patel, S.G., Boyle, J.O., Hudis, C.A., and Dannenberg, A.J. (2016). White adipose tissue inflammation and cancer-specific survival in patients with squamous cell carcinoma of the oral tongue. Cancer *122*, 3794–3802. https://doi.org/10.1002/cncr.30251.
62. York, A.G., Williams, K.J., Argus, J.P., Zhou, Q.D., Brar, G., Vergnes, L., Gray, E.E., Zhen, A., Wu, N.C., Yamada, D.H., et al. (2015). Limiting cholesterol biosynthetic flux spontaneously engages type I IFN signaling. Cell *163*, 1716–1729. https://doi.org/10.1016/j.cell.2015.11.045.
63. Xia, Y., Xie, Y., Yu, Z., Xiao, H., Jiang, G., Zhou, X., Yang, Y., Li, X., Zhao, M., Li, L., et al. (2018). The mevalonate pathway is a druggable target for vaccine adjuvant discovery. Cell *175*, 1059–1073.e21. https://doi.org/10.1016/j.cell.2018.08.070.

STAR★METHODS

KEY RESOURCES TABLE

REAGENT or RESOURCE	SOURCE	IDENTIFIER
Antibodies		
Alexa Fluor© 700 anti-mouse CD45	BioLegend	Cat# 103128; RRID: AB_493715
APC/Cy7 anti-mouse TCR beta chain	BioLegend	Cat# 109220; RRID: AB_893624
Brilliant Violet 605 anti-mouse TCR γ/δ	BioLegend	Cat# 118129; RRID: AB_2563356
Brilliant Violet 421 anti-mouse CD4	BioLegend	Cat# 100543; RRID: AB_10898318
FITC anti-mouse CD8a	BioLegend	Cat# 100706; RRID: AB_312745
APC anti-mouse IFN-γ	BioLegend	Cat# 505810; RRID: AB_315404
PE/Cy7 anti-mouse PD-1	BioLegend	Cat# 135216; RRID: AB_10689635
NLRC3 Antibody	Abcam	Cat# ab77817, RRID:AB_2042467
HRP Anti-beta Actin antibody [AC-15]	Abcam	Cat# ab49900; RRID: AB_867494
Goat anti-rabbit IgG–HRP Antibody	Abcam	Cat# ab97051; RRID: AB_10679369
Goat anti-mouse IgG–HRP Antibody	Abcam	Cat# ab97023; RRID: AB_10679675
Anti-Acly antibody	LSBio	Cat# LS-B13453
Phospho-TBK1/NAK (Ser172) Antibody	Cell Signaling Technology	Cat# 5483S; RRID: AB_10693472
TBK1/NAK Antibody	Cell Signaling Technology	Cat# 3504S; RRID: AB_225566
Phospho-STING (Ser365) Antibody	Cell Signaling Technology	Cat# 72971S; RRID: AB_2799831
STING Antibody	Cell Signaling Technology	Cat# 13647S; RRID: AB_2732796
Anti-FLAG M2 Antibody	Cell Signaling Technology	Cat# 14793; RRID:AB_2572291
Anti-HA-Tag Antibody	Cell Signaling Technology	Cat# 3724; RRID:AB_1549585
phospho-IRF-3 (Ser396) Antibody	Cell Signaling Technology	Cat# 4947S; RRID: AB_823547
IRF-3 Antibody	Cell Signaling Technology	Cat# 4302S; RRID: AB_1904036
Bacterial and virus strains		
One Shot™ Stbl3™ Chemically Competent E. coli	Invitrogen	Cat# C737303
One Shot™ TOP10 Chemically Competent E. coli	Invitrogen	Cat# C404003
Chemicals, peptides, and recombinant proteins		
PBS, pH 7.4	ThermoFisher	Cat# 10010023
2′3′-cGAMP	InvivoGen	Cat# tlrl-nacga23-1
2′3′-cGAM(PS)$_2$ (Rp/Sp)	InvivoGen	Cat# tlrl-nacga2srs
ISD naked	InvivoGen	Cat# tlrl-isdn
Poly(dA:dT)	InvivoGen	Cat# tlrl-patn-1
LPS	InvivoGen	Cat# 00-4976
500 mL DMEM	Corning	Cat# 10-013-CV
HyClone Characterized Fetal Bovine Serum	Cytiva	Cat# SH30071.03IH25-40
Penicillin streptomycin (10,000 U/mL)	ThermoFisher	Cat# 15-140-122
IMDM	Gibco	Cat# 12440053
Ham's F-12 Nutrient Mix	ThermoFisher	Cat# 11765054
Puromycin, 100 mg	InvivoGen	Cat# ant-pr-1
Insulin, Human Recombinant, Zinc Solution 5 mL	Invitrogen	Cat# 12585014
Hydrocortisone	Sigma-Aldrich	Cat# H0888-1G
Recombinant murine GM-CSF	PeproTech	Cat# 315-03
Recombinant mouse IFN-γ	BioLegend	Cat# 575302
Epidermal growth factor, human recombinant	EMD Millipore	Cat# 01-107
RPMI-1640 1× With L-glutamine	Corning	Cat# MT10040CV
Bovine Serum Albumin	MilliporeSigma	Cat# A9418

(*Continued on next page*)

Continued

REAGENT or RESOURCE	SOURCE	IDENTIFIER
Palmitic acid, ≥99%	Sigma-Aldrich	Cat# P0500
Palmitoleic acids, ≥98.5%	Sigma-Aldrich	Cat# P9417
Myristic acids, ≥99%	Sigma-Aldrich	Cat# M3128
Sodium oleate, ≥99%	Sigma-Aldrich	Cat# O7501-1G
Sodium hydroxide 1.0 N Solution	Sigma-Aldrich	Cat# S2770-100ML
Tris-HCl pH 8.0	ThermoFisher	Cat# BP1758500
Triton X-100	Sigma-Aldrich	Cat# X100
Sodium dodecyl sulfate	Sigma-Aldrich	Cat# 74255-250G
Sodium chloride	Sigma-Aldrich	Cat# S3014-5KG
Sodium deoxycholate	Sigma-Aldrich	Cat# D6750
Sodium fluoride	Sigma-Aldrich	Cat# 201154
Mini Protease Inhibitor Cocktail	Roche	Cat# 11836170001
Halt™ Phosphatase Inhibitor Cocktail	Thermo-Fisher	Cat# 78420
Retrieval buffer	Biogenex	Cat# Hk081-20k
Harris Hematoxylin	Fisher Scientific	Cat# NC9520196
Isopropanol	Fisher Scientific	Cat# A426P-4
Oil Red O – Isopropanol Solutio	Rowley Biochemical	Cat# H-503-1B
3,3′-Diaminobenzidine tablets (DAB)	Sigma Aldrich	Cat# D4168-5SET
alamarBlue Cell Viability Reagent	Invitrogen	Cat# DAL1025
ACK lysing buffer	Gibco	Cat# A1049201
Ficoll-Paque PLUS density gradient media	GE Healthcare	Cat# 17-1440-03
Critical commercial assays		
RNeasy® Plus Mini Kit	Qiagen	Cat# 74134
QIAshredder	Qiagen	Cat# 79654
High-Capacity cDNA Reverse Transcription Kit	Applied Biosystems	Cat# 4368814
RNAse inhibitor	Applied Biosystems	Cat# 8080119
LumiKine™ Xpress mIFN-β 2.0 kit	Invivogen	Cat# luex-mifnbv2
Tnf-α Mouse ELISA kit	Invivogen	Cat# BMS6073
CellTrace™ CFSE Cell Proliferation Kit	Invitrogen	Cat# C34554
EasySep Dead Cell Removal (Annexin V) Kit	STEMCELL Technologies	Cat# 17899
Anti-HA Agarose	Thermo Fisher Scientific	Cat# 26181
anti-FLAG M2 Affinity gel	Millipore Sigma	Cat# A2220
VECTASTAIN® ABC Kits (HRP)	Vectastain	Cat# PK-4001
Cholesterol/Cholesterol Ester-Glo™ Assay	Promega	Cat# J3190
Murine EasySep CD8+ T cell isolation kit	Stemcell Technologies	Cat# 19853
Dynabeads CD3/CD28	Gibco	Cat# 11456D
Zombie Aqua™ Fixable Viability Kit	BioLegend	Cat# 423101
Deposited data		
Single-cell RNA-Seq dataset	NCBI Sequence Read Archive	PRJNA756027
Experimental models: Cell lines		
PCI-13	University of Pittsburgh	RRID:CVCL_C182
FaDu	ATTC	RRID:CVCL_1218
UMSCC22A	University of Michigan	RRID:CVCL_7731
MOC2-E6/7	Harvard University	RRID:CVCL_ZD33
Experimental models: Organisms/strains		
Mouse: C57BL/6J	Jackson Laboratory	RRID:IMSR_JAX:000664
Mouse: B6.129S7-*Rag1*^{tm1Mom}/J	Jackson Laboratory	RRID: IMSR_JAX:002216
Mouse: B6.129S2-*Ifnar1*^{tm1Agt}/Mmjax	Jackson Laboratory	RRID:IMSR_JAX:002216

(*Continued on next page*)

Continued

REAGENT or RESOURCE	SOURCE	IDENTIFIER
Oligonucleotides		
NLRC3 sgRNA: 5′-CCGGGTCTCCATCACTATCG-3′	Integrated DNA Technologies	N/A
qPCR primer sequences	Table S2, the current study	N/A
Recombinant DNA		
pcDNA3.1 Empty Vector	Lei et al.[51] Immunity	
lentiCRISPRv2 puro	Addgene	RRID:Addgene_98290
NLRC3-CRISPR/Cas9	The current study	N/A
pLKO.1-shIfnar1	Sigma-Aldrich	Clone ID# TRCN0000067279
pLKO.1-shNlrc3	Sigma-Aldrich	Clone ID# TRCN0000249396
pLKO.1–empty vector	Sigma-Aldrich	Cat# SHC001V
pPAX2 packaging plasmid	University of North Carolina at Chapel Hill	Dr. Jenny P.Y. Ting
VSV-G envelop plasmid	University of North Carolina at Chapel Hill	Dr. Jenny P.Y. Ting
pcDNA3–human NLRC3–HA	University of North Carolina at Chapel Hill	Dr. Jenny P.Y. Ting
pcDNA3.1–human STING–HA	University of Miami	Dr. Glen N. Barber
pcDNA3.1–human FLAG-STING	University of Miami	Dr. Glen N. Barber
pcDNA3.1–murine STING–HA	University of Miami	Dr. Glen N. Barber
Software and algorithms		
FlowJo v10.7.2	FlowJo, LLC	FlowJo
Gen5 program v2.09	Agilent	Gen5
ImageJ	ImageJ	ImageJ
Other		
Metric Vernier caliper	United Scientific™	Cat# S139595
PicoLab® Laboratory Rodent Diet	LabDiets	Cat# 5L0D
Rodent Diet With 60 kcal% Fat	Research Diets	Cat# D12492
Tissue Culture Cell Scraper 25cm	Sarstedt	Cat# 50-101-128
Serum Gel collection tubes	Sarstedt	Cat# 20.1344
0.45μm PES filter	Fisher Scientific	Cat# SLHVR33RS
Cell strainer, 70 μm	Corning	Cat# CLS431751
96-well Flat Clear Bottom Black Polystyrene TC-treated Microplates	Corning	Cat# 3904

RESOURCE AVAILABILITY

Lead contact

Further information and requests for resources and reagents should be directed to and will be fulfilled by the lead contact, Yu Leo Lei (leiyuleo@umich.edu).

Materials availability

Plasmids, cell lines, and unique reagents and materials are available to investigators at non-profit institutions upon the establishment of a material transfer agreement. Reagent sharing with investigators at for-profit institutions will be implemented after a licensing agreement.

Data and code availability

- The single-cell RNA-Seq dataset of TILs from lean and obese hosts has been deposited at the NCBI Sequence Read Archive with BioProject ID PRJNA756027 (http://www.ncbi.nlm.nih.gov/bioproject/756027). The dataset is publicly available as of the date of publication. The accession number is listed in the key resources table.
- This paper does not report original code.
- Any additional information required to reanalyze the data reported in this work paper is available from the lead contact upon request.

EXPERIMENTAL MODEL AND SUBJECT DETAILS

Animal studies

All animal handling and procedures were performed in accordance with the animal ethics and protocols approved by the Institutional Animal Care and Use Committee (IACUC) at the University of Michigan (PRO00008517 and PRO00010232). Male and female C57BL/6J (RRID:IMSR_JAX:000664), female *Ifnar1*$^{-/-}$ (RRID: IMSR_JAX:002216), and female *Rag1*$^{-/-}$ (RRID:IMSR_JAX:002216) mice were purchased from The Jackson Laboratory at eight weeks of age and group-housed under specific pathogen–free conditions in a temperature- and light-controlled environment. *Ifnar1*$^{-/-}$ mice were subsequently backcrossed nine generations into the C57BL/6J line. To establish the obese mouse model, C57BL/6J mice were fed either a normal diet (5L0D, LabDiet, 24.6% protein, 11.4% fat, 57.3% carbohydrate, 4.09 kcal/g) or a 60% kcal% fat diet (D12492, Research Diets, 20% protein, 60% fat, 20% carbohydrate, 5.21 kcal/g) for twelve weeks before tumor implantation. As sex is not a known prognosticator for HNSCC, both sexes were used. Syngeneic HNSCC models were established by inoculation of one million empty vector control, shNLRC3, or wild-type MOC2-E6/E7 cells subcutaneously in the right flank of mice. To test drug efficacy, three weekly doses of either mock (PBS, 100 μL) or 2′3′-cGAM(PS)$_2$ (Rp/Sp) (50 μg/100 μL; catalog no. tlrl-nacga2srs, InvivoGen) were administered intratumorally. Notably, littermate controls of the same sex were randomly assigned to treatment groups. Beginning on day seven after tumor implantation, tumors were measured using a digital Vernier caliper every two-to-three days, and tumor volume was calculated according to the formula 1/2 (length × width^2). All mice were euthanized at the indicated time points. After euthanasia, tumors, TILs, livers, sera, and spleens of the mice were harvested for subsequent analysis.

Cell lines and treatments

The HNSCC cell line PCI-13 (RRID:CVCL_C182) was derived from a male patient and acquired from the University of Pittsburgh. The HNSCC cell line UMSCC22A (RRID:CVCL_7731)was derived from a female patient and acquired from the University of Michigan. The HNSCC cell line FaDu (RRID:CVCL_1218) was derived from a male patient and purchased from ATCC. All human cell lines were authenticated and maintained in DMEM (10-013-CV, Corning) supplemented with 10% FBS (Gibco, Life Technologies), 100 U/mL penicillin (Gibco), and 100 mg/mL streptomycin (Gibco). The MOC2-E6/E7 (RRID:CVCL_ZD33) cell line was derived from a female mouse and acquired from Harvard University. MOC2-E6/E7 was authenticated and cultured in 60% IMDM (SH30228.01, HyClone) with 30% F12 nutrient mix (11764-054, Gibco), 5% FBS, 4 μg/mL puromycin, 5 μg/mL insulin, 40 ng/mL hydrocortisone, 5 ng/mL EGF, 100 U/mL penicillin, and 100 mg/mL streptomycin. We generated *NLRC3*-targeting CRISPR-Cas9 lentiviruses, using a single-guide RNA (sgRNA): 5′-CCGGGTCTCCATCACTATCG-3′. NLRC3–knockout cells were established by transduction of HNSCC cells (PCI-13, FaDu) with the *NLRC3*-targeting CRISPR/Cas9 lentivirus. Control cells were transduced with empty vector virus that did not express the sgRNA sequence. qPCR on human *NLRC3* was performed to validate the knockdown efficiency. EV-MOC2-E6/E7 and shNlrc3-MOC2-E6/E7 cell lines were transduced with empty vector control (EV) or shNlrc3-expressing lentiviruses (MilliporeSigma) followed by enhanced puromycin selection due to MOC2-E6/E7 cell-intrinsic low puromycin resistance (concentration of 120 μg/mL). Puromycin was purchased from InvivoGen (ant-pr-1). qPCR on murine *Nlrc3* was performed to validate the knockdown efficiency. Type I interferon pathway activation was assessed *in vitro* via the following agonists: 2′3′-cGAMP (tlrl-nacga23-1, InvivoGen); ISD naked (tlrl-isdn, InvivoGen); Poly(dA:dT) (tlrl-patn-1, InvivoGen); pcDNA3.1–human STING–HA and pcDNA3.1–murine STING–HA were provided by Glen N. Barber of the University of Miami.

Bone marrow-derived macrophages (BMDMs) isolation and differentiation

BMDMs were isolated from both adult female and male mice to assess type-I interferon responses in immune compartments. In brief, mice were euthanized, after which the two posterior femurs, tibias, and fibulas were resected from mice, using scissors and forceps sterilized with 70% ethanol, and placed within the biosafety cabinet. Bone ends were subsequently cut, and bone marrow was flushed out in sterile PBS using a 27G needle (305109, BD) and filtered through a 70-μm cell strainer to achieve a single-cell suspension. Cells were spun down and resuspended in 5 mL of BMDM differentiation media (RMPI media with L-glutamine containing 20% heat-inactivated FBS, L-929 cell supernatant, and 1% penicillin/streptomycin). Cells were split into five 100 mm tissue culture-treated Petri dishes containing a final volume of 10 mL per plate. On day three post-plating, an additional 10 mL differentiation media was added to aid cellular growth. On day six post-plating, media was removed, and dishes were washed once with 1× PBS. Cells were then gently removed from the plate in 5 mL 1× PBS using a 25 cm cell scraper, spun down, and counted. Cells were plated for experimental use in 6-well tissue culture plates, 0.5 × 10^6 cells/well in 2 mL BMDM culture media (RPMI media with L-glutamine containing 20% heat-inactivated FBS and 1% penicillin/streptomycin).

Peritoneal macrophages isolation and differentiation

Peritoneal macrophages were isolated from male mice to assess myeloid cell sensitivity to agonists of the STING-IFN-I pathway. Mice were euthanized and mounted supine on a Styrofoam block. Using scissors and forceps, sterilized with 70% ethanol, the inner lining of the peritoneal cavity was exposed and injected with 5 mL of ice-cold PBS containing 3% FBS using a 27G needle. Briefly, the peritoneum was massaged to dislodge attached cells. A 25G needle was used to collect the fluid from the cavity and then inspected for blood contamination. An incision was made in the peritoneal cavity to collect any remaining fluid using a pipette. Samples were combined with regards to their groups, obese (n = 6) and lean (n = 6), spun down, and then plated in a 12-well tissue-culture dish,

1.6×10^6 cells/well in 1 mL culture media (RPMI media with L-glutamine containing 20% heat-inactivated FBS and 1% penicillin/streptomycin). The following day, media was aspirated, and the remaining adherent cells were used for downstream assays.

METHOD DETAILS

Preparation of fatty acid conjugates

To test the effects of free saturated and unsaturated fatty acids in modulating the type I interferon response, we prepared palmitate-BSA, palmitoleate-BSA, myristate-BSA, and sodium oleate-BSA conjugates. In brief, to prepare the BSA solution, 10% (w/v) fatty acid-free bovine albumin (A9418-5G, MilliporeSigma) was gradually added to ultrapure water at 52°C with gentle agitation until the BSA was fully dissolved. To prepare palmitate, palmitoleate, and myristate, palmitic acids (P0500, Sigma-Aldrich), palmitoleic acids (P9417, Sigma-Aldrich), and myristic acids (M3128, Sigma-Aldrich) were added to 0.1M NaOH (S2770, Sigma-Aldrich) and heated to 70°C until fully dissolved, yielding a concentration of 100 mM. Likewise, sodium oleate (O7501, Sigma-Aldrich) was added to ultrapure water at 55°C to yield a concentration of 100 mM. To conjugate fatty acids to BSA, the 100 mM stocks of palmitate, palmitoleate, myristate, and sodium oleate were added to 10% BSA at a ratio of 1:9 and heated at 55°C for 10 min. After conjugation, both the 10% (w/v) BSA solution and fatty acid-BSA solutions were filter-sterilized using a 0.45 μm PES filter (SLHVR33RS, Fisher Scientific), aliquoted, and stored at −20°C. Before use, solutions were warmed to 37°C. For final use, 200 μM of both fatty acid-BSA conjugates were used.

Gene expression qPCR & ELISA

For qPCR, total RNA was extracted using QIAshredder and the RNeasy Plus Mini Kit (catalog 79654 and 74134, respectively; Qiagen). RNA concentration was measured using a Nanodrop Spectrophotometer (Thermo Fisher Scientific). RNA was reverse-transcribed into cDNA using High-Capacity cDNA Reverse Transcription Kit and RNAse inhibitor (4368814 and N8080119, Applied Biosystems). The primers were synthesized by Integrated DNA Technologies. The primer sequences are shown in Table S2. For ELISA, supernatant from treated MOC2-E6/E7, BMDMs, and peritoneal macrophages was collected 16 h post-treatment with agonists of the type I interferon pathway. Protein levels of murine Ifn-β and Tnf-α in the supernatant were quantified using a LumiKine™ Xpress mIFN-β 2.0 kit (luex-mifnbv2, Invivogen) and Tnf-α Mouse ELISA kit (BMS6073, Invitrogen). The bioluminescent intensity was measured using a Synergy H1 microplate reader (Agilent) and Gen5 program (version 2.09), and three technical replicates per sample were examined simultaneously.

Immunoblotting assays

Whole-cell lysates per condition were harvested on ice in RIPA buffer (50 mM Tris-HCl pH 8.0 [BP1758500, ThermoFisher], 1% Triton X-100 [X100, Sigma-Aldrich], 0.05% SDS [74255-250G, Sigma-Aldrich], 0.25% deoxycholate [D6750, Sigma-Aldrich], 150 mM NaCl [S3014-5KG, Sigma-Aldrich], and 50 mM NaF [201154, Sigma-Aldrich]) supplemented with a protease inhibitor cocktail (11836170001, Roche) and Halt Phosphatase Inhibitor Cocktail (78420, Thermo Fisher Scientific). Once collected, the samples were rotated at 4°C for 30 min and centrifuged at 13,000 g for 10 min at 4°C. Lysates were blotted on NuPAGE™ 4 to 12%, Bis-Tris, 1.0 mm Gel (NP0323BOX, ThermoFisher). Proteins from lysates were blotted using the following antibodies: NLRC3 antibody (ab77817, RRID:AB_2042467, Abcam), Phospho-TBK1/NAK (Ser172) Antibody (5483S, RRID: AB_10693472, Cell Signaling Technology), TBK1/NAK Antibody (3504S, RRID: AB_225566, Cell Signaling Technology), Phospho-STING (Ser365) Antibody (72971S, RRID: AB_2799831, Cell Signaling Technology), STING Antibody (13647S, RRID: AB_2732796, Cell Signaling Technology), phospho-IRF-3 (Ser396) Antibody (4947S, RRID: AB_823547, Cell Signaling Technology), IRF-3 Antibody (4302S, RRID: AB_1904036, Cell Signaling Technology), and anti-beta actin antibody (ab49900, RRID: AB_867494, Abcam). The secondary antibodies anti-rabbit IgG–HRP Antibody (ab97051, RRID: AB_10679369, Abcam) and anti-mouse IgG–HRP Antibody (ab97023, RRID: AB_10679675, Abcam) were used as needed. The dilutions for the primary antibodies were as follows: β-actin, 1:100,000; and 1:1000 for other antibodies. All antibodies were diluted in 5% skim milk. To assess the interaction between NLRC3 and STING, HA-NLRC3 and FLAG-STING plasmids were transfected into PCI-13, FADU, and UMSCC22A cells. Whole-cell lysates were harvested on ice in NP40 buffer (50 mM Tris-HCl pH 8.0, 150 mM NaCl, and 0.1% NP-40) supplemented with a protease inhibitor cocktail (11836170001, Roche) and Halt Phosphatase Inhibitor Cocktail (78420, Thermo Fisher Scientific). FLAG-STING and HA-NLRC3 proteins were pulled down by using the anti-FLAG M2 Affinity gel (A2220, Millipore Sigma) and Anti-HA Agarose (26181, Thermo Fisher Scientific). After three gently washes, immunoprecipitated protein complexes were resuspended in 1× LDS sample buffer, boiled at 95°C for 5 min, then were blotted using the following antibodies: anti-FLAG M2 Antibody (14793, RRID:AB_2572291, Cell Signaling Technology) and anti-HA-Tag Antibody (3724, RRID:AB_1549585, Cell Signaling Technology).

Histology, immunohistochemistry, and oil red O staining

After formalin fixation and paraffin embedding, specimens were sectioned, deparaffinized on a 58°C drying bench for 20 min, and then rehydrated. Retrieval buffer (Hk081-20k, Biogenex) was used for antigen unmasking and 0.3% hydrogen peroxide was used for quenching the endogenous peroxidase. Sections were blocked with 5% goat serum in PBS-T for 1 h and incubated with an anti-Acly antibody (LS-B13453, LSBio) or an anti-Nlrc3 antibody (ab77817, RRID:AB_2042467, Abcam) at 4°C overnight. After washing twice in PBS-T buffer for 5 min each, the specimens were incubated with a secondary antibody (1:100 dilution) at room

temperature for 30 min. Then we used an ABC kit (PK-4001, Vectastain) for the addition of Avidin-Biotinylated HPR Complex. Sections were incubated with DAB (D4168-5SET, Sigma) for 3 min and stopped in water. For the Oil Red O staining, liver specimens were embedded in OTC and sectioned. After air-dry at room temperature, the slides were fixed in 10% Neutral Buffered Formalin. Then they were rinsed in water and dipped in 60% isopropanol (A426P-4, Fisher Scientific). The slides were placed in the Oil Red O – Isopropanol Solution (H-503-1B, Rowley Biochemical), washed twice, and then stained with Harris Hematoxylin (NC9520196, Fisher Scientific) for 15 s. The images were analyzed using ImageJ.

AlamarBlue assay

Empty vector control or shNlrc3-MOC2-E6/E7 cells were seeded at a density of 500 cells per well in 96-well microplates with a flat black bottom (3904, Corning). Every 24 h from day 1 to day 4, corresponding wells were supplemented with 10% alamarBlue (DAL1025, Invitrogen), and the plate was subsequently incubated at 37°C for 4 h. The fluorescence intensity (excitation 560, emission 590 nm) of these wells was measured using a Synergy H1 microplate reader (Agilent)and Gen5 program (version 2.09), and five replicates per group were examined simultaneously.

Quantitation of serum cholesterol levels

Serum cholesterol was measured using a luminescent plate assay (J3190, Promega) according to the manufacturer's instructions. Blood was collected from mice prior to euthanasia by submandibular bleeds and collected in Microvette 500 Serum Gel collection tubes (20.1344, Sarstedt). The luminescent intensity was measured using the Synergy H1 microplate reader (Agilent) and the Gen5 program (version 2.09).

Flow cytometry

Immune cells from tumors and spleens were purified. Tumors were excised from mice, weighed, and minced into pieces, followed by tissue dissociation and passage through a 70-μm cell strainer to obtain a single-cell suspension. Spleens were processed by mechanical dissociation, followed by lysis of red blood cells with ACK lysing buffer (A10492-01, Gibco). Ficoll-Paque PLUS (17-1440-03, GE Healthcare Life Sciences) was added to the bottom of each tube containing single-cell suspensions in RPMI1640, followed by density-gradient centrifugation to purify immune cells. In general, approximately 1×10^6 tumor-infiltrating lymphocytes were extracted from tumors post-Ficoll purification. Cells were subsequently stained for multi-fluorophore flow cytometric analysis with the following antibodies: anti-CD45 (clone 30-F11, BioLegend), anti-TCRβ chain (clone H57-597, BioLegend), anti-TCRγδ (clone GL3, BioLegend), anti-CD4 (clone RM4-5, BioLegend), anti-CD8 (clone 53-6.7, BioLegend), anti-IFN-γ (clone XMG1.2, BioLegend), anti-PD-1 (clone 29F.1A12, BioLegend), anti-CD11b (clone M1/70, BioLegend), and anti-Ly-6G (RB6-8C5, BioLegened). Cells were also stained for viability using Zombie Aqua (423101, BioLegend) diluted 1:1000 in PBS at 4°C for 30 min. Flow cytometric acquisition and initial compensation were conducted on a Beckman Coulter CytoFLEX and BioRad ZE5 Cell Analyzer. Approximately 0.5×10^5 tumor-infiltrating lymphocytes were acquired per experiment. FlowJo version 10 software was used for compensation and data analysis.

MDSC functional assay

In vitro generation of MDSCs involved first harvesting bone marrow from lean and obese mice following the previously described protocol. Once cells were obtained in a single cell suspension, cells were incubated in MDSC differentiation media (RMPI-1640, 1% L-glutamine, 10% heat-inactivated fetal bovine serum, and 50uM β-mercaptoethanol 1% penicillin-streptomycin) containing 200 U/mL recombinant murine GM-CSF (315-03, PeproTech) for four days. Following this, the cells were treated with a combination of 0.1 μg/mL LPS (00-4976, Invitrogen) and 100 U/mL IFN-γ (575302, BioLegend) for 16 h to activate the MDSCs. Cells were stained using the following flow cytometric panel: Zombie Aqua (423101, BioLegend), anti-CD11b (clone M1/70, BioLegend), and anti-Ly-6G (RB6-8C5, BioLegened). FACS sorting on Beckman MoFlo Astrios Cell Sorter was used to isolate granulocytic MDSCS. Spleens from age-matched C57BL6/J mice were harvested, on the same day of MDSC sorting, to purify $CD8^+$ T-cells for co-culture with MDSCs. First, spleens were collected in ice-cold PBS and then smeared against a 70-μM cell strainer to obtain a single-cell suspension. $CD8^+$ T-cells were isolated using a murine EasySep $CD8^+$ T cell isolation kit (19853, Stemcell Technologies) and then stained using 5 μM CFSE Violet Proliferation dye (C34554, Invitrogen) for 20 min in a 37°C incubator. MDSCs were dispended into wells containing labeled $CD8^+$ T-cells and then stimulated with Dynabeads CD3/CD28 (11456D, Gibco) for four days to enable T cell expansion. Cells were then stained using the following panel: Zombie Aqua (423101, BioLegend), anti-CD8 (clone 53-6.7, BioLegend), and anti-CD11b (M1/70, BioLegened). CFSE dilution in $CD8^+$ T-cells was analyzed by flow cytometry. MDSCS were also isolated from tumors grown in lean and obese mice. First, the tumors were harvested in RPMI1640 media, mashed, and processed using tumor dissociation media (RPMI1640, 1 mg/mL Collagenase I, 250 U/mL Collagenase IV, and 20 U/mL Dnase) for 30 min in 37°C water bath. Cells were stained using Zombie Aqua viability dye (423101, BioLegend) and the following antibodies: anti-CD45 (clone 30-F11, BioLegend), anti-CD11b (clone M1/70, Biolegend), and anti-Gr1 (clone RB6-8C5, Biolegend). Cells were sorted using Invitrogen Bigfoot Cell Sorter. At the same time, $CD8^+$ T-cells were acquired from the spleens of lean mice and labeled with CFSE proliferation dye as previously described. MDSCs were dispensed into wells containing CFSE-labeled T-cells from and incubated with Dynabeads CD3/CD28 for four days; after which, cells were stained using the previously described flow panel and analyzed for CFSE dilution using flow cytometry.

Single-cell immune profiling

Whole tumor lysate was treated with ACK Lysing Buffer (A1049201, ThermoFisher), then processed through an EasySep Dead Cell Removal (Annexin V) Kit (17899, STEMCELL Technologies). The cell suspension was submitted in 1× PBS +0.04% BSA for 10× Genomics 3′-single-cell processing and RNA-Seq at a depth of at least 30,000 reads per cell. We utilized the following criteria to select high-quality transcriptomes: (i) the qualified cells must have unique feature counts between 200 and 7,500; (ii) the mitochondrial reads must be fewer than 10%; (iii) the transcriptomes must have unique molecular identifiers counts over 500. We integrated 5,154 high-quality transcriptomes for downstream analyses. We utilized the sctransform tool to remove the library size effect and the mutual nearest neighbor algorithm to remove the batch effect for final integration. We selected the top 2,025 genes with the highest cell-to-cell variation as well as features to stabilize the immune population structure. The single-cell dataset is deposited to the NCBI Sequence Read Archive with a BioProject ID PRJNA756027.

QUANTIFICATION AND STATISTICAL ANALYSIS

Statistical analysis between two independent groups was made using unpaired, two-tailed Student's t-tests. Comparisons between more than two groups were made using two-way ANOVA with Šidák's multiple-comparisons post hoc analysis. Tumor burden between groups was compared using the generalized estimating equation model unless otherwise specified. Statistical significance is indicated in all figures according to the following scale: *$p < 0.05$; **$p < 0.01$; ***$p < 0.001$; and ****$p < 0.0001$. All graphs are presented as the mean ± SEM. To test the differentially expressed genes between T-cells separated from the tumors in lean control mice and the tumors grown in obese mice, we employed the R-package "stats" and performed the non-parametric Wilcoxon test.